Supplementary Information

Wafer-Scale Synthesis of Metal-Oxide Nanonetworks for Ultra-Sensitive, Sub-Second Hydrogen Sensing Chips

Jiyong Zhou[1#], Sixing Xu[1,2#]*, Hui Li[1], Shunyang Zhou[3], Tianliang Meng[3], Siya Liu[3], Xiaoting Tan[3], Yuxuan Liang[1], Mingquan Zhang[3], Zhibiao Zhu[3], Jianyou Dai[3], Long Cheng[3], Yiliu Wang[3], Xiaohong Wang[4], Wenbo Ding[5], Changsheng Wu[6], Wanli Duan[7], Rui Li[7], Shenghua Ding[7], Qian Li[8]*, Lei Liao[1], Lei Shan[3]*

[1]College of Semiconductors (College of Integrated Circuits), Hunan University, Changsha, China, 410082

[2]Yuelushan Center for Industrial Innovation, Changsha, China, 410082

[3]School of Physics & Electronics, Hunan University, Changsha, China, 410082

[4]School of Integrated Circuits, Tsinghua University, Beijing, China, 100084

[5]Shenzhen International Graduate School, Tsinghua University, Shenzhen, China, 518055

[6]Department of Material Science & Engineering, National University of Singapore, Singapore 117575

[7]Dongting Laboratory, Hunan Institute of Agricultural Product Processing and Quality Safety, Hunan Academy of Agricultural Sciences, Changsha, China, 410125

[8]School of Physics & Electronics, Hunan Normal University, Changsha, China, 410081

[#]These authors contribute equally.

Correspondence and requests for materials should be addressed to S. X., Q. L. & L. S. (email: xusx2021@hnu.edu.cn, liqianl@hunnu.edu.cn, leishan@hnu.edu.cn).

Table of contents

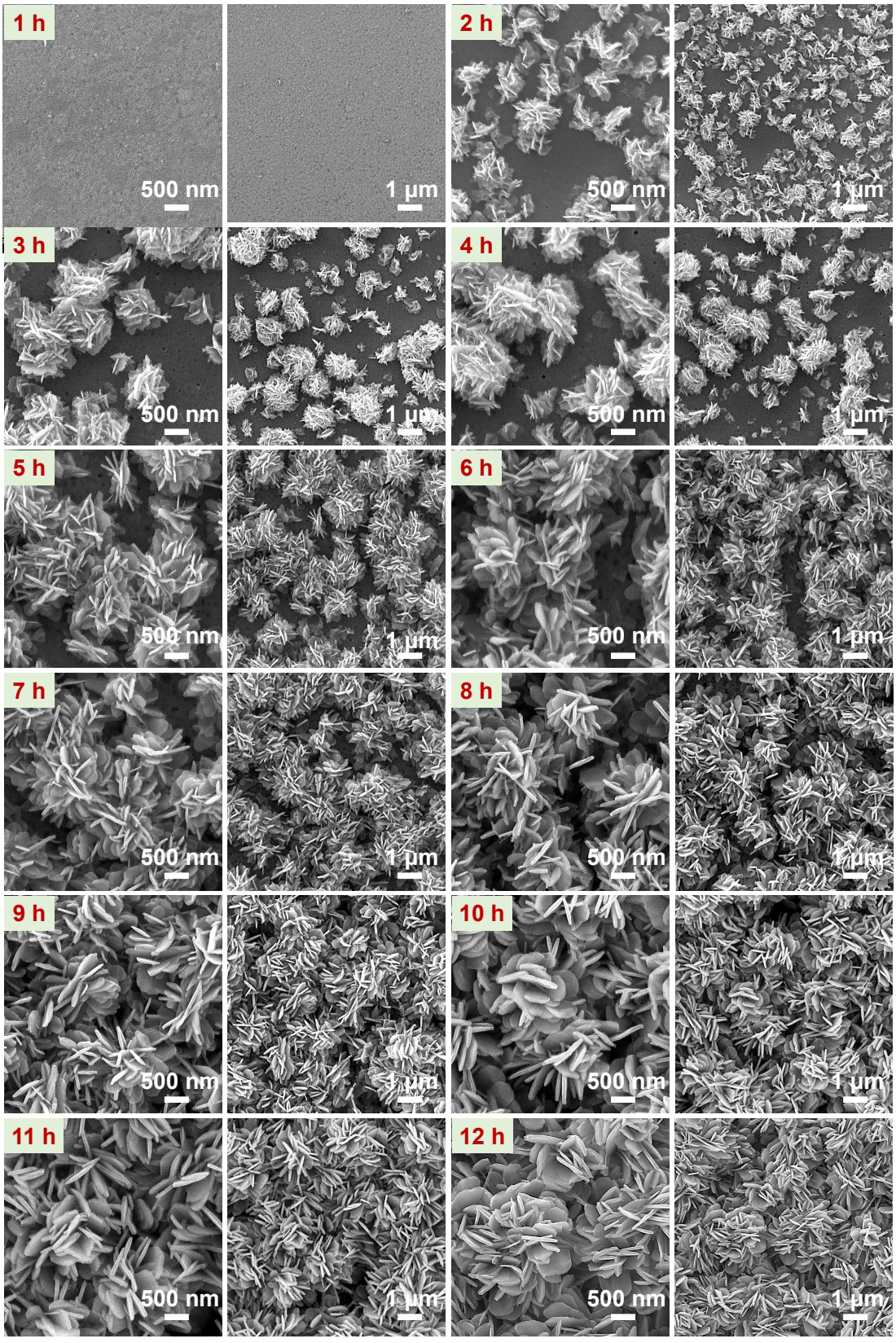

Supplementary Figure 1| SEM images of the surface structure of WO_3 films changing with etching time.

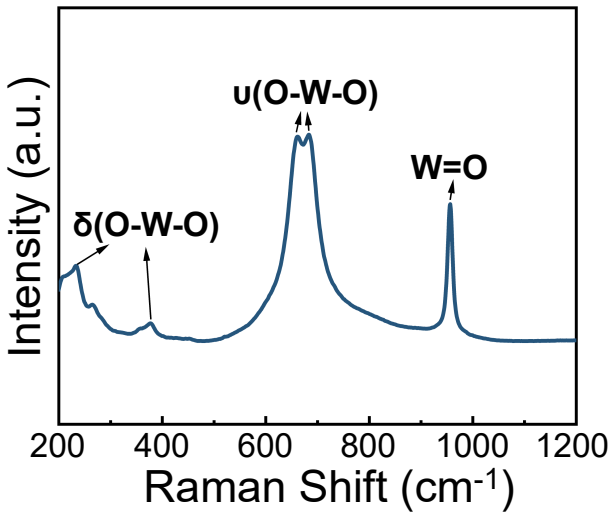

Supplementary Figure 2| Raman spectrum of $WO_3 \cdot 2H_2O$.

As shown in the figure, the Raman spectrum of the sample exhibits a pronounced and sharp peak at 956 cm^{-1}, which can be attributed to the stretching vibration of the terminal W=O double bond. The doublet peaks observed at 661 cm^{-1} and 683 cm^{-1} correspond to the stretching vibrations of W–O–W bridging bonds, characteristic of the connectivity within WO_6 octahedra, indicating an intact octahedral framework in the sample. In the low wavenumber region, additional characteristic peaks at 377 cm^{-1} and 233 cm^{-1} are assigned to the bending modes of O–W–O linkages, further suggesting good crystallinity and a stable crystal structure. These observed vibrational modes are consistent with the expected molecular configuration and bonding interactions within the $WO_3 \cdot 2H_2O$ structure[1, 2].

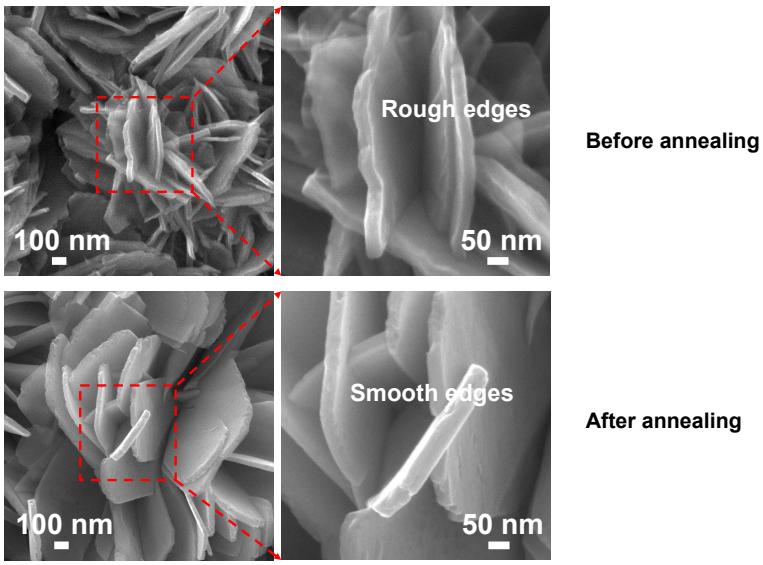

Supplementary Figure 3| SEM images of the morphology of WO_3 nanosheets before and after annealing.

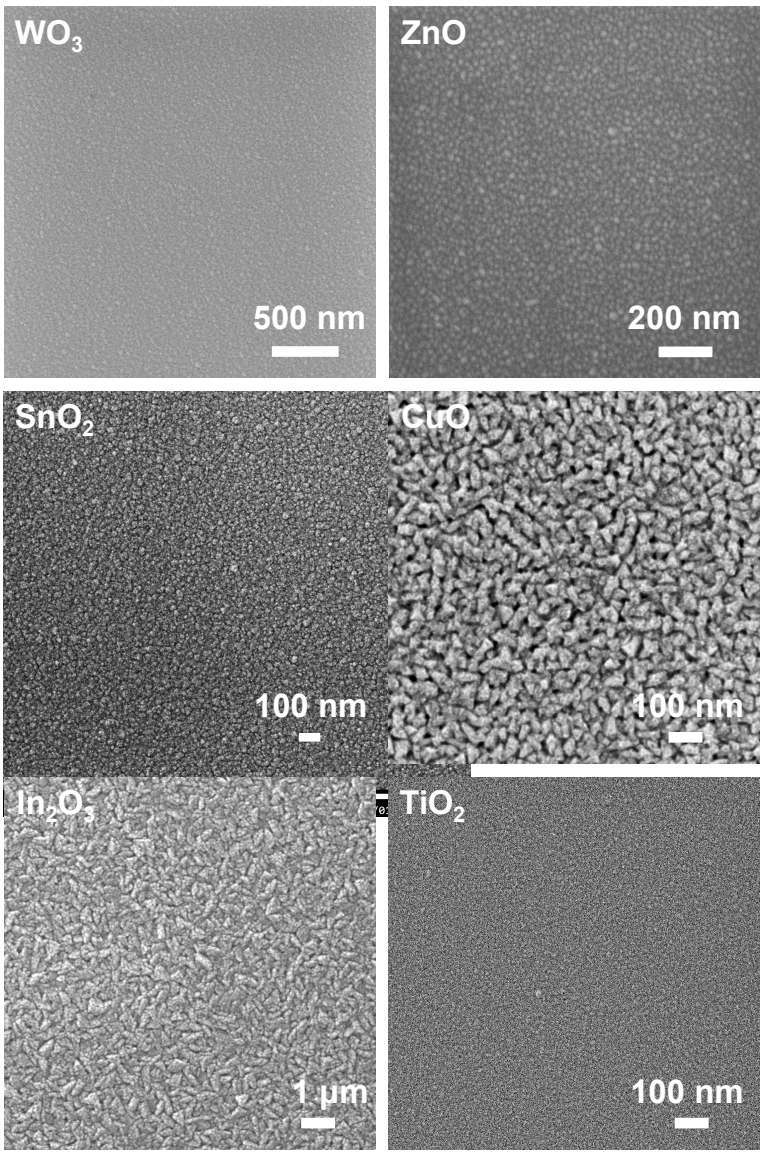

Supplementary Figure 4| SEM images of the morphology of various samples before etching.

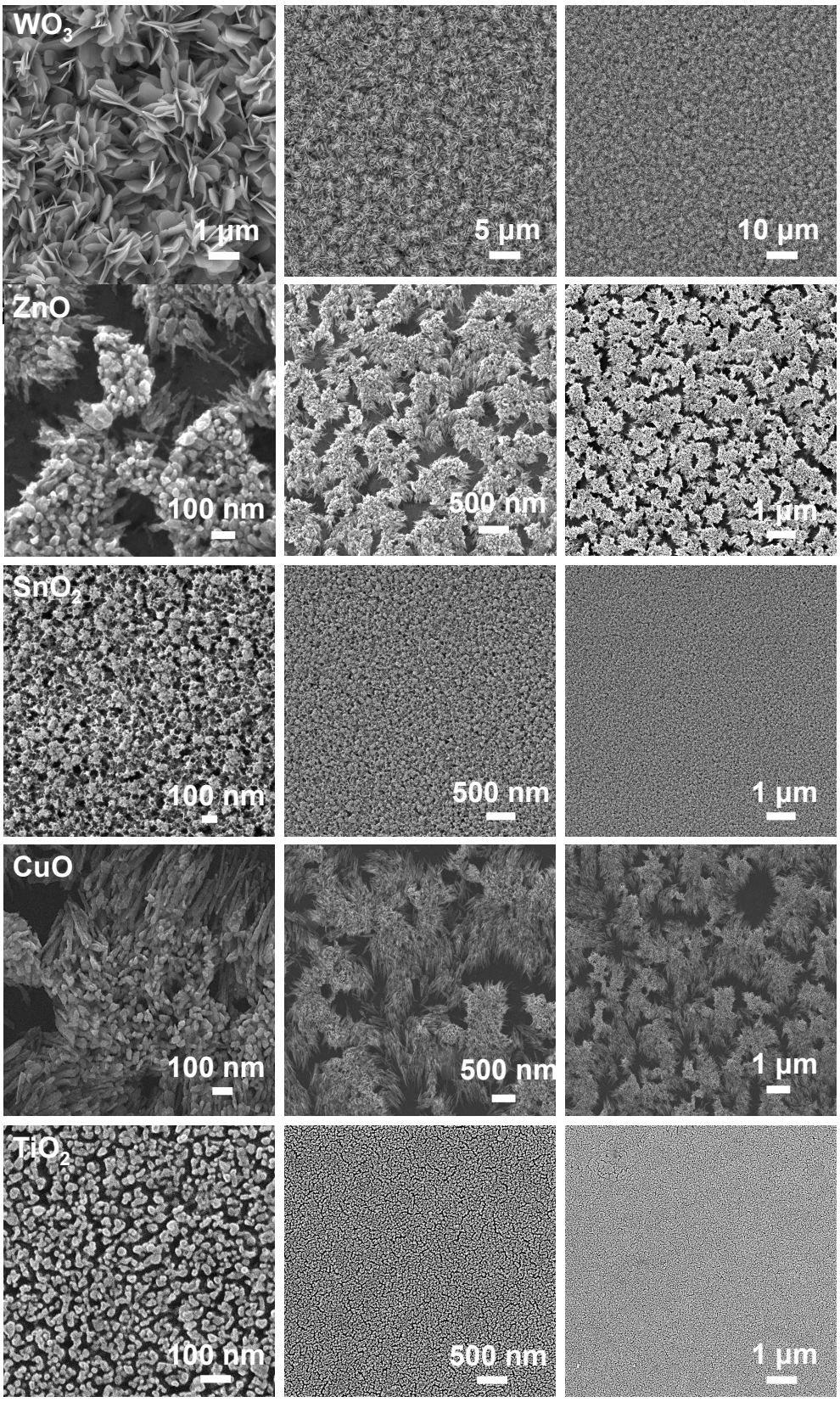

Supplementary Figure 5| SEM images of the morphology (other scales) of various samples after etching.

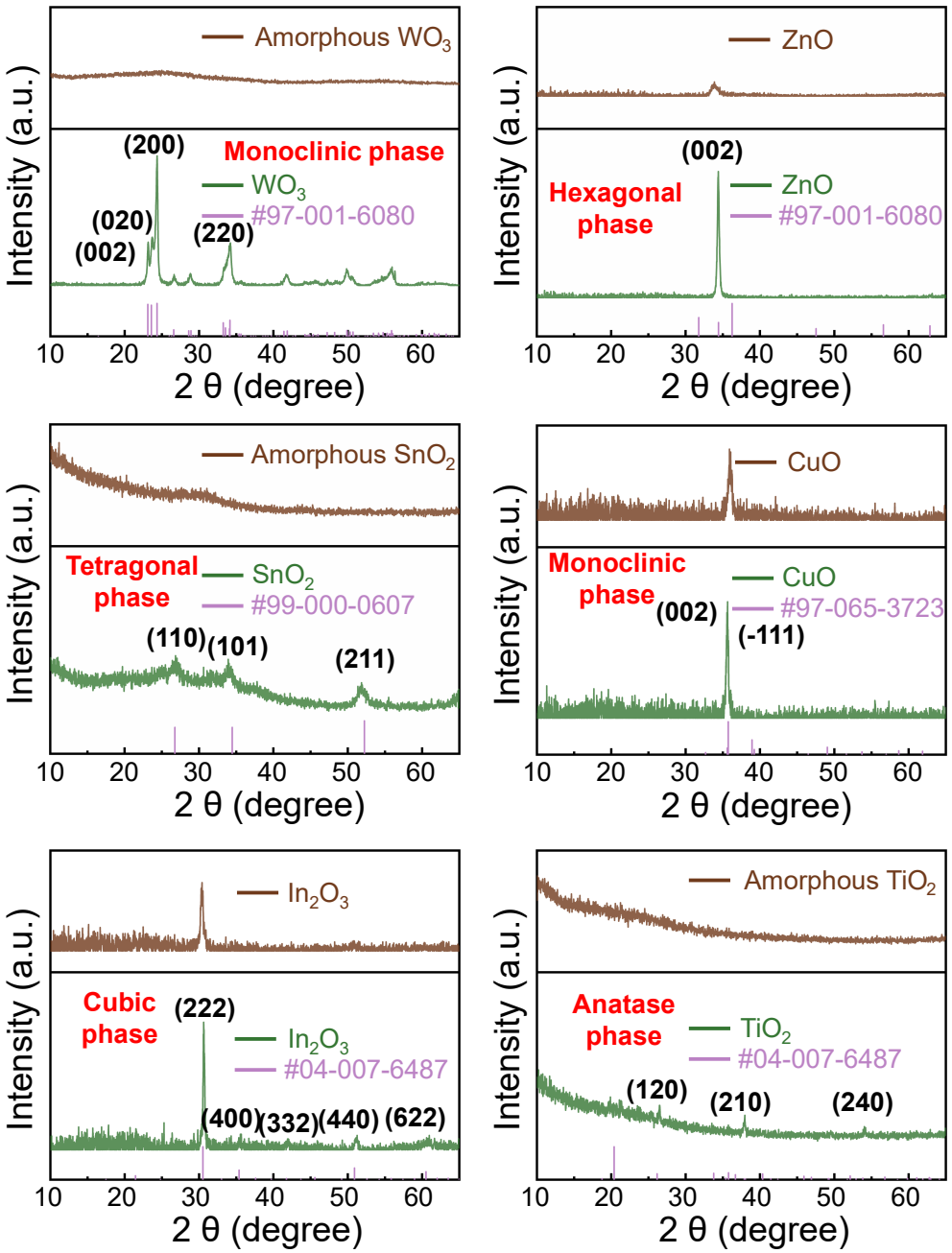

Supplementary Figure 6| XRD patterns of various samples after sputtering or annealing.

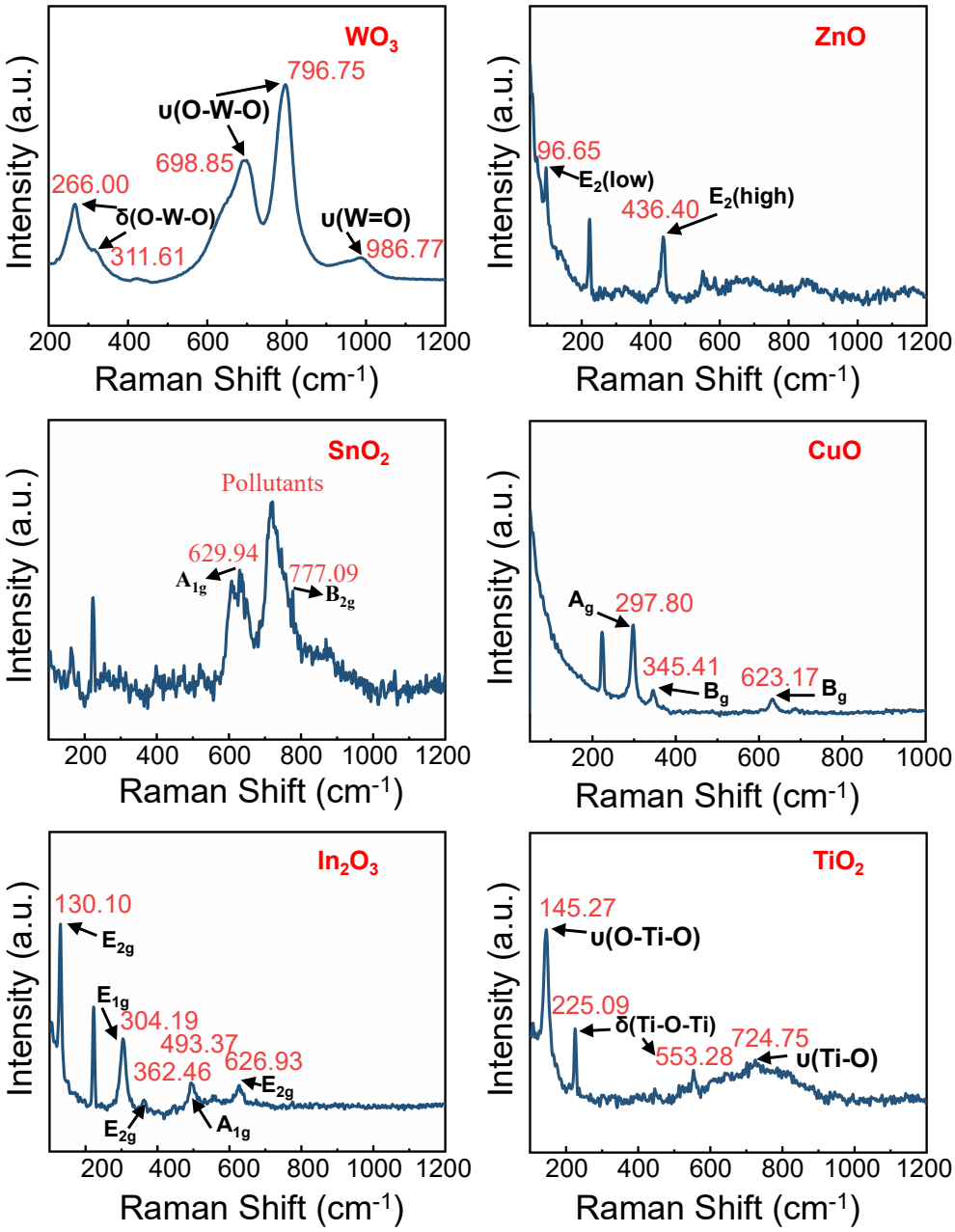

Supplementary Figure 7| Raman spectra of various samples after annealing.

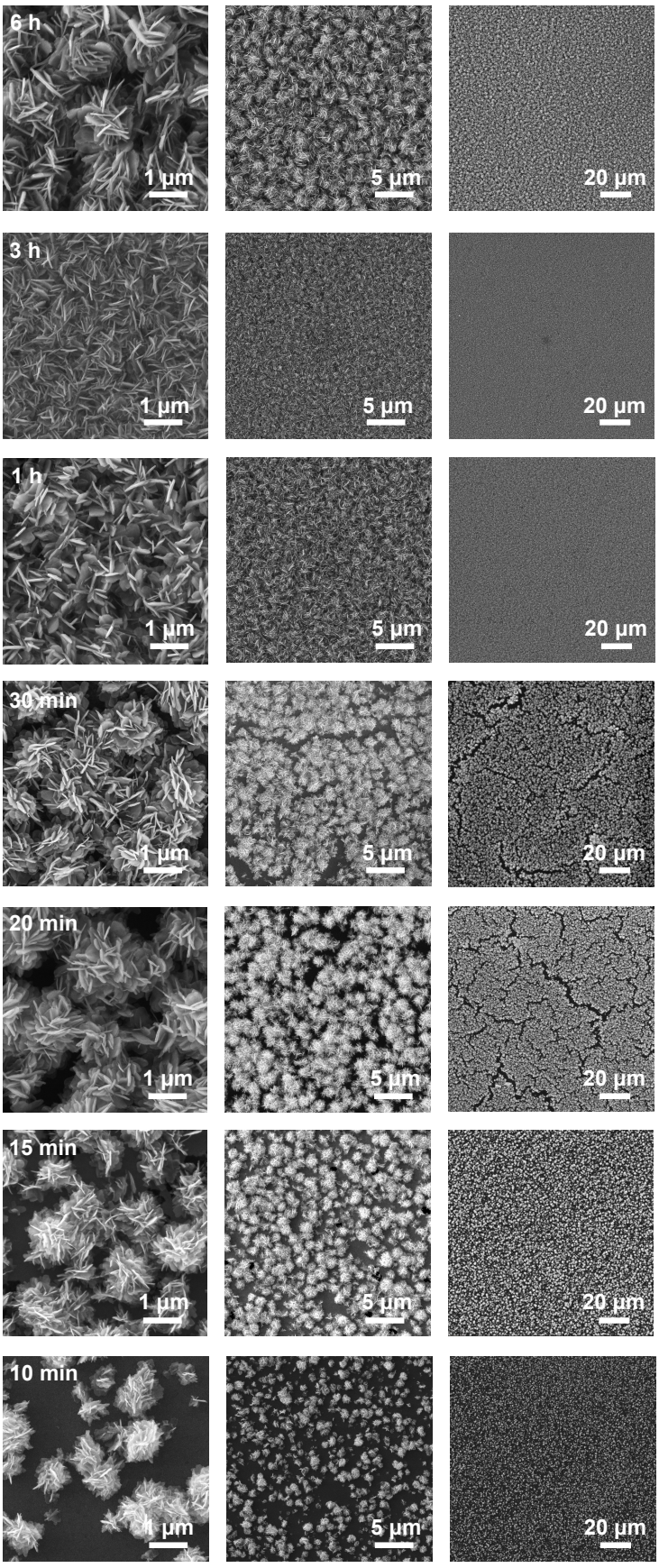

Supplementary Figure 8| Nanomorphology after etching corresponding to different sputtering times.

By varying only the sputtering duration (i.e., the deposited WO_3 loading; 6 h, 3 h, 1 h, 30 min, 20 min, 15 min, and 10 min), we obtained a series of post-etch morphologies. As the deposition time decreases, the etched films become progressively more sparse. At 15 min, nearly all nanospheres assembled from WO_3 nanosheets are discrete and well isolated, and their areal number density is not lower than that of the 10-min sample. The 15-min specimen therefore yields a nanostructured sensing layer with pronounced gas-transport pathways, in which the constituent nanosheets are almost fully exposed to the ambient, providing the structural basis for subsequent high-performance hydrogen sensing.

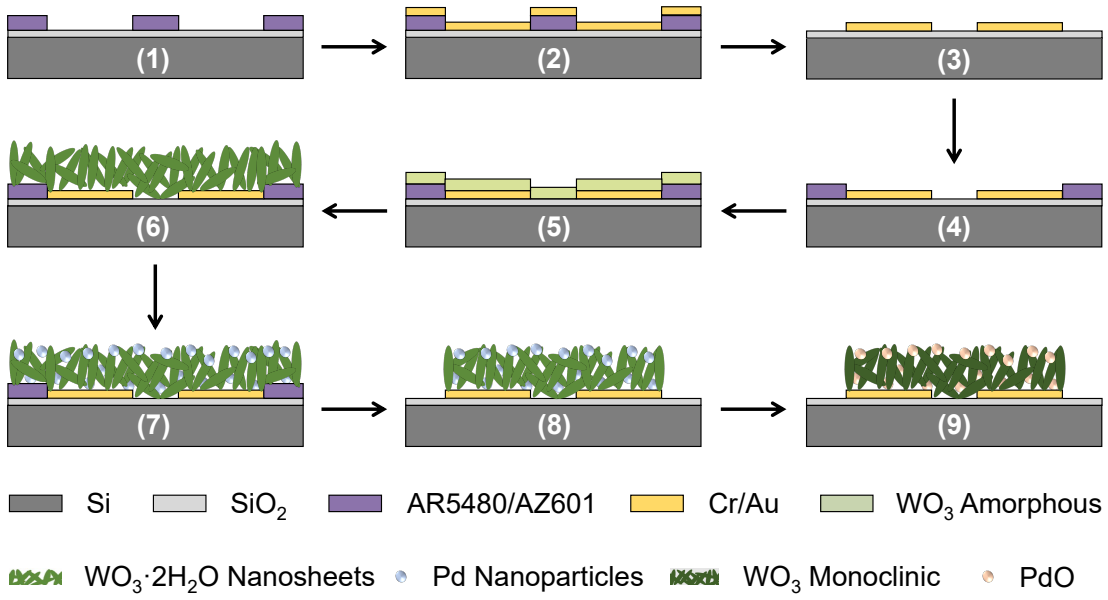

Supplementary Figure 9| Illustration of the entire microfabrication process of PdO/WO_3 sensors.

Detailed fabrication steps:

(1) Use the 4-inch Si (500 μm)/SiO_2 (300 nm) wafer as the substrate. Pattern the wafer substrate with the photoresist (AR5480/AZ601, 2000/3000 rpm, 150 ℃, 3 min/100 ℃, 2min) and Mask No.1 using ultraviolet photolithography machine (EVG 610, 200 mJ/cm^2) to define the region of interdigitated electrodes (150 μm width, 50 μm electrode gap).

(2) Deposit Cr (10 nm)/Au (40 nm) as the adhesive layer and current collector of sensors using the Vacuum evaporation.

(3) Immerse the wafer in the acetone for 10 minutes to lift off the photoresist/Cr/Au to form the interdigitated electrodes of sensors.

(4) Defined the sensing layer region (1.3 mm length, 0.75 mm width) with Mask No. 2 UV and photoresist (same as above) using the ultraviolet photolithography (EVG 610, 200 mJ/cm^2).

(5) Magnetron sputtering WO_3 (Bound with copper back target, DC 60 W) for 15 minutes to create sensing layer of sensors without heating the substrate.

(6) Immerse the wafer in the hydrochloric acid HCl (0.5 mol/L) for chemical etching for 12 h, and the dense WO_3 sensing layer slowly formed a nanosheet structure.

(7) Conventional magnetron sputtering of Pd (DC 40 W) decorates Pd nanoparticles onto the nanosheets without heating the substrate.

(8) Immerse the wafer in the acetone for 10 minutes to lift off the photoresist/Pd-WO_3 to finish the pattern of sensing layer.

(9) The wafer was annealed at 400 °C in air for 2 h.

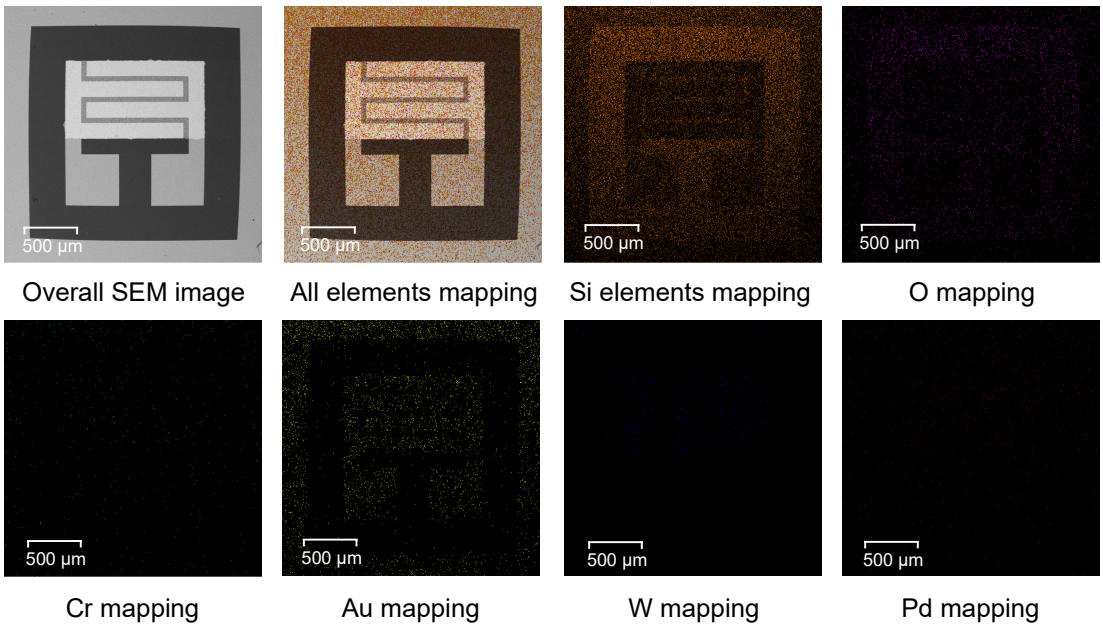

Supplementary Figure 10| EDS elemental mapping of a single sensor device.

It shows that all constituent elements appear from bottom to top in the sequence prescribed by the fabrication stack. W and Pd are primarily localized on the test electrodes, consistent with the device design, indicating that the PdO/WO_3 nanosheet array is indeed formed within the boundary region of the electrodes. The Cr and Pd maps are relatively faint, mainly due to their low loading and the large field of view used for imaging.

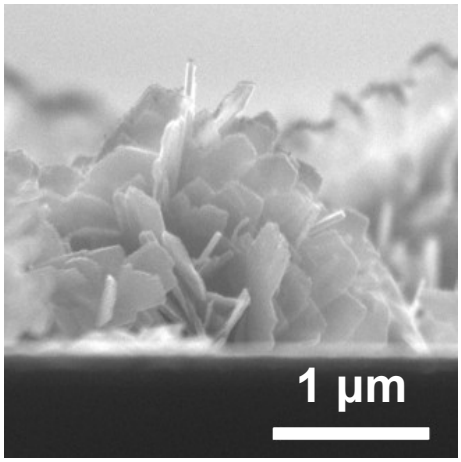

Supplementary Figure 11| The cross-section images of the PdO/WO_3-20s sensor.

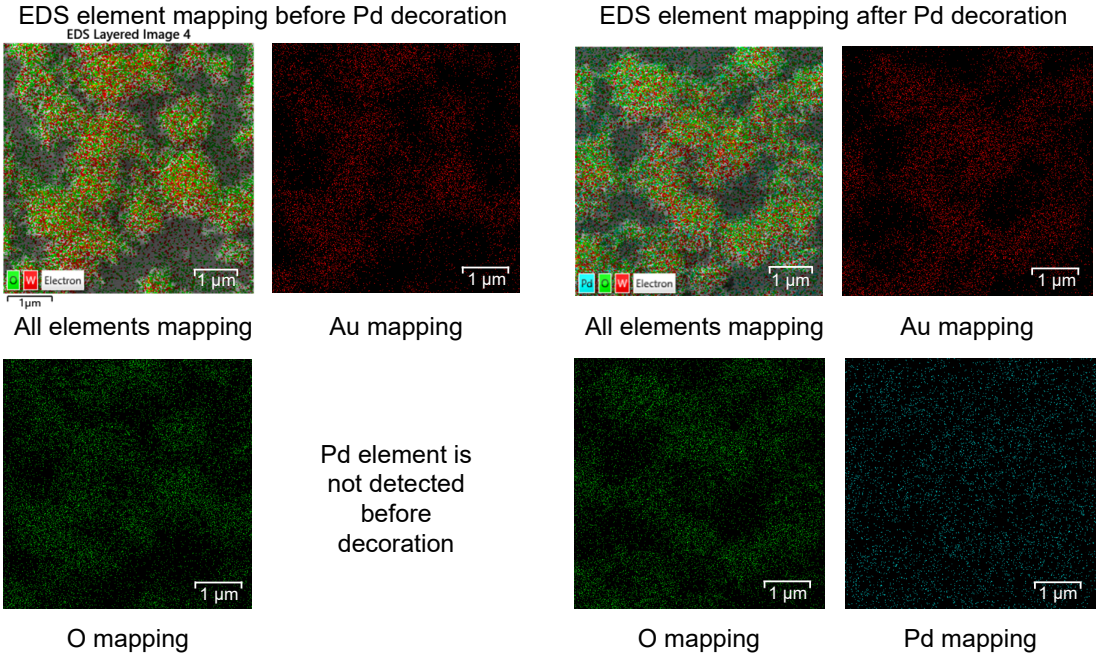

Supplementary Figure 12| EDS element mapping images of the WO_3 NSs before Pd decoration (Left) and after Pd decoration (Right).

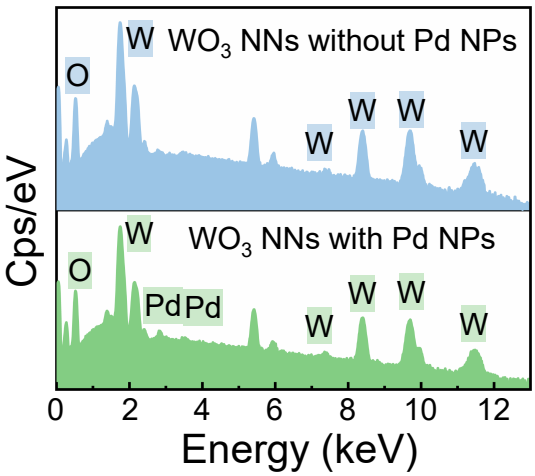

Supplementary Figure 13| EDS spectrum of the WO_3 NSs before Pd decoration and after Pd decoration.

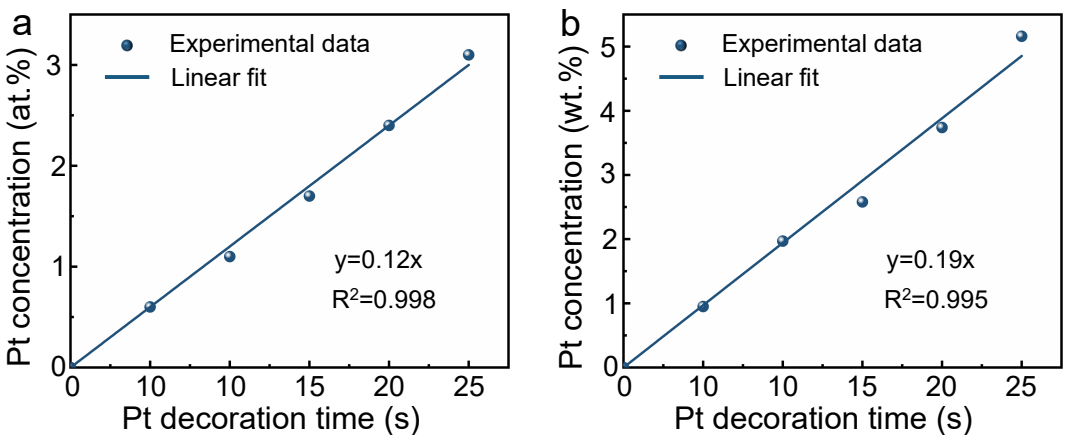

Supplementary Figure 14| Calculated atom percentage (a) and normalized weight percentage (b) of Pd from EDS data as a function of Pd decoration time.

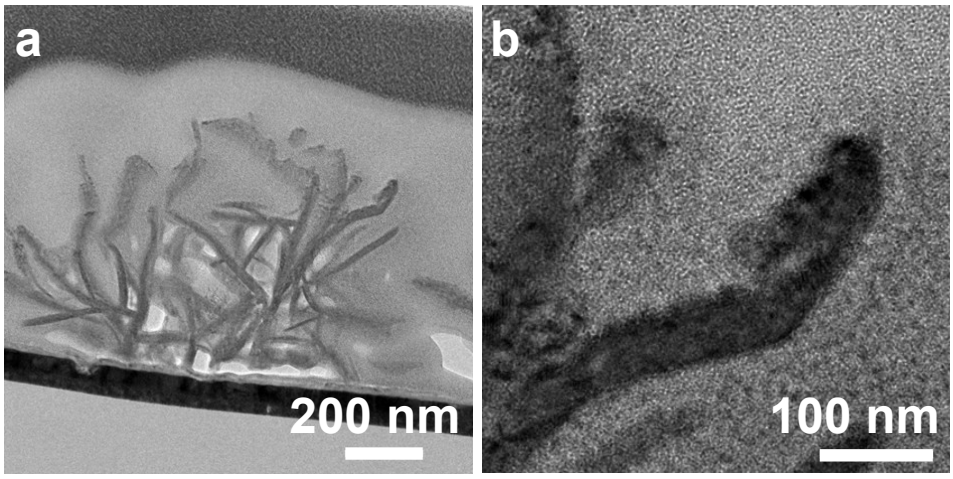

Supplementary Figure 15| a Overall and b TEM images of PdO/WO_3 nanosheets (the Pt layer on top of the layer stack are part of the FIB lamella preparation).

The TEM images in Supplementary Fig. 15 (prepared by FIB slicing) further provide direct information about the PdO/WO_3 nanosheet structure. Supplementary Fig. 15a shows that the individual nanosphere structures composing the nanosheets grow divergently from the substrate surface, forming a high-aspect-ratio sheet-like aggregate. The higher magnification TEM image (Supplementary Fig. 15b) highlights the localized contrast enhancement features of individual nanosheet fragments, with dense dark regions visible along the edges of the sheets, indicating that PdO is attached to the surface of the WO_3 sheets. In the Pd/WO_3 composite material, Pd is typically dispersed in the form of PdO NSs under air annealing conditions, and this dispersion characteristic is consistent with previously reported PdO/WO_3 systems.

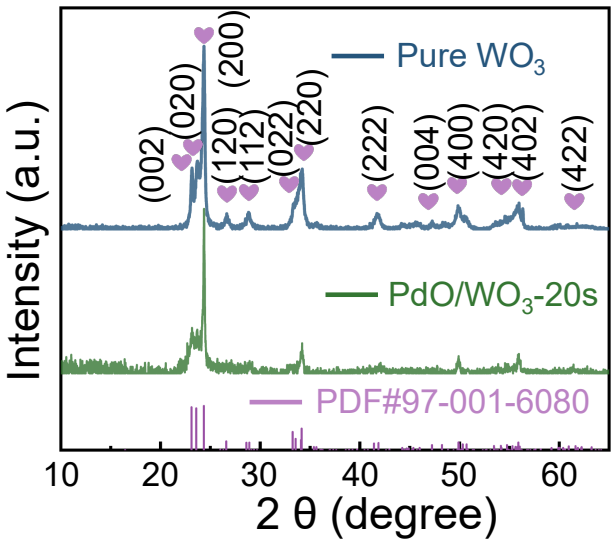

Supplementary Figure 16| XRD patterns of WO_3 and PdO/WO_3-20s nanosheets.

All peaks can be indexed to monoclinic WO_3 (PDF#97-001-6080). No discernible diffraction peaks associated with Pd or PdO are observed, and the main WO_3 reflections exhibit no obvious peak shift, indicating that at the Pd loading level used in this work, Pd is present predominantly as highly dispersed, low-content oxide species on the surface rather than being incorporated into the WO_3 lattice[3].

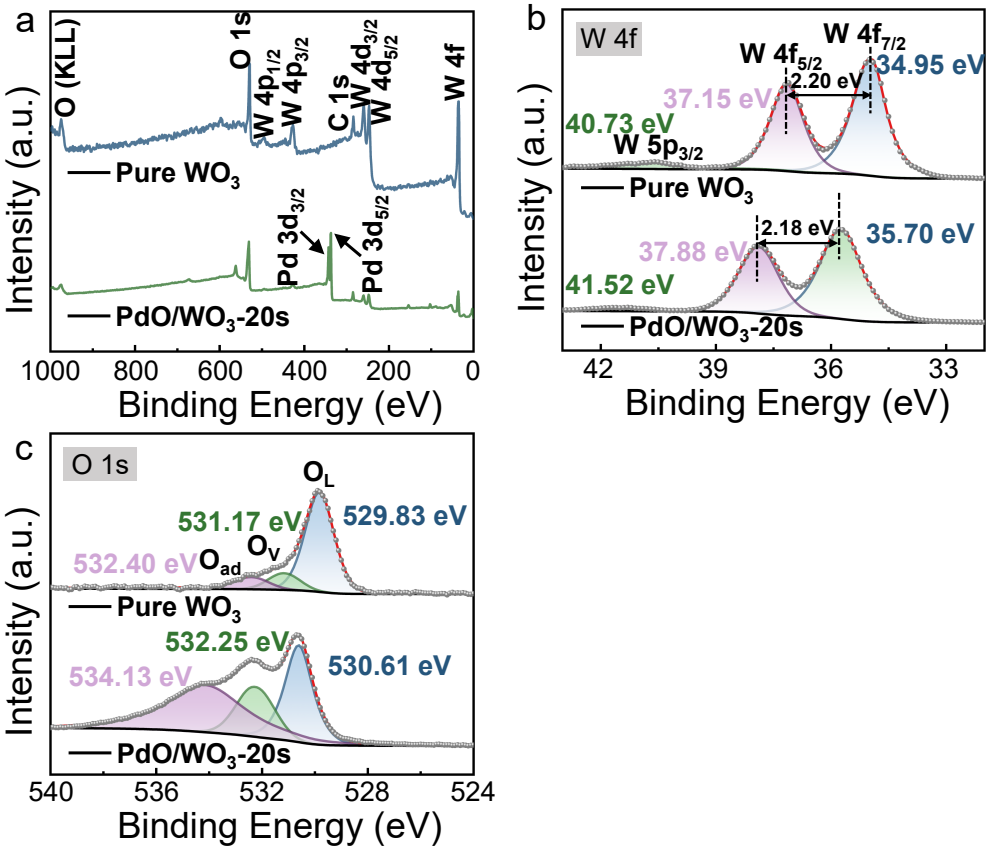

Supplementary Figure 17| XPS spectra of the WO_3 and PdO/WO_3-20s nanosheets: a Full spectra, b W 4f and c O 1s.

Compared with pristine WO_3 films, the survey spectrum of PdO/WO_3-20s shows a pronounced Pd 3d feature, confirming the coexistence of W, O and Pd in the sample (Supplementary Fig. 17a). As shown in Supplementary Fig. 17b, the W $4f_{7/2}$ and W $4f_{5/2}$ peaks of pristine WO_3 are located at 34.95 eV and 37.15 eV, respectively, whereas in PdO/WO_3-20s they shift to higher binding energies of 35.70 eV and 37.88 eV. The spin–orbit splitting remains ~2.2 eV, consistent with a W^{6+}-dominated valence state. The overall positive shift in binding energy indicates that Pd incorporation slightly decreases the electron density around W through interfacial charge transfer and surface catalytic oxidation effects[4]. The O 1s spectrum (Supplementary Fig. 17c) can be deconvoluted into three components: lattice oxygen (O_L) (pristine WO_3: 529.83 eV; PdO/WO_3-20s: 530.61 eV), oxygen-vacancy-related oxygen (O_V) (531.17 → 532.25 eV), and adsorbed oxygen (O_{ad}) (532.40 → 534.13 eV). Notably, the area fractions of the high-binding-energy components (O_V and O_{ad}) increase markedly in PdO/WO_3-20s (Supplementary Table 3), indicating that Pd modification substantially enriches surface defect oxygen and chemisorbed oxygen species. Extensive studies have shown that these reactive oxygen species serve as key sites for charge exchange with target gases such as H_2 in metal-oxide gas-sensing reactions, and can amplify the resistance change by modulating the surface depletion layer thickness[5, 6].

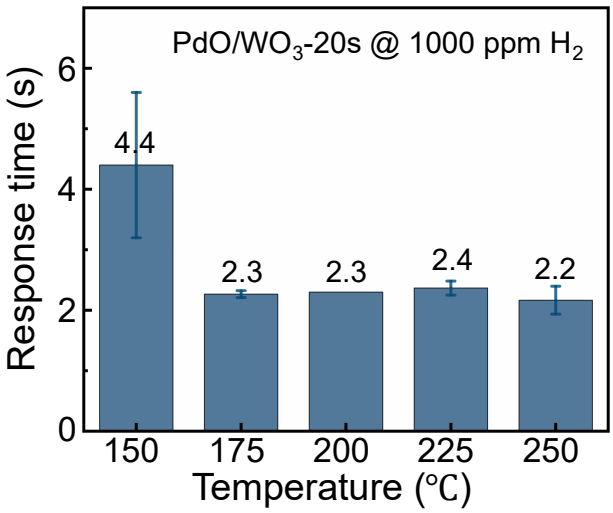

Supplementary Figure 18| Relationship between response time and operating temperature for the PdO/WO_3-20s sensor to 1000 ppm H_2.

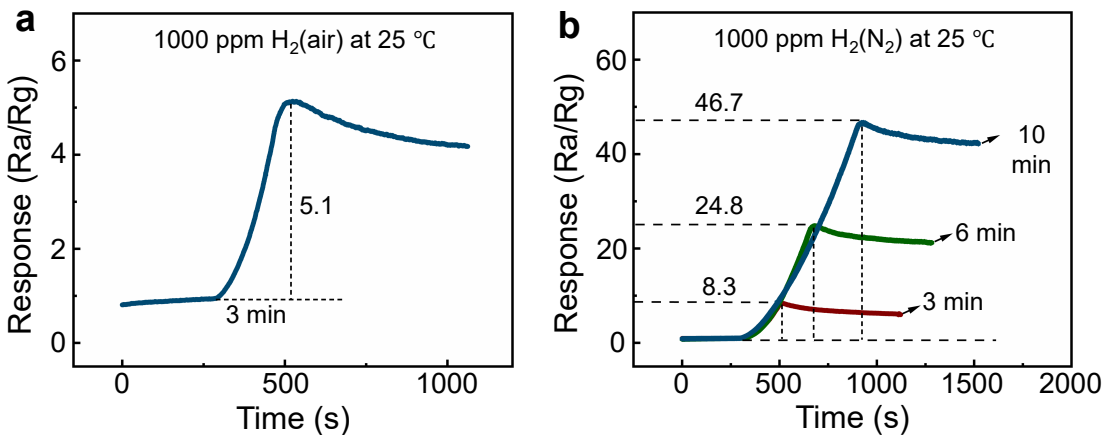

Supplementary Figure 19| Room-temperature (25 °C) dynamic response of the PdO/WO_3-20s sensor to 1000 ppm H_2 under different background atmospheres: (a) in air; (b) in N_2 with different exposure durations (3, 6 and 10 min).

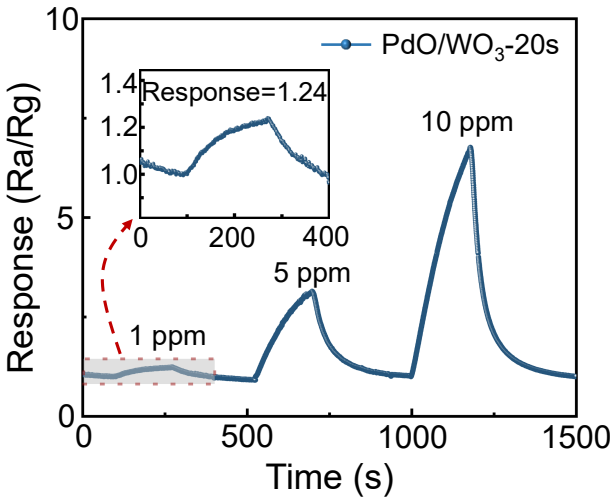

Supplementary Figure 20| The dynamic response-recovery curves of PdO/WO_3-20s sensor to different concentrations (1-10 ppm) of H_2 at 175 ℃.

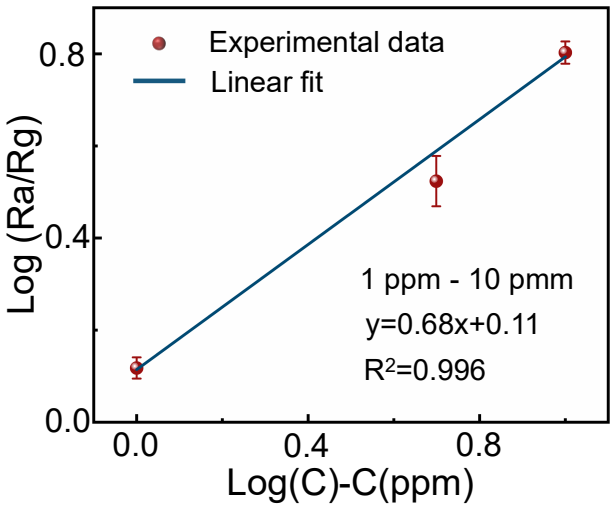

Supplementary Figure 21| The corresponding log (Ra/Rg)-log(C) fitted curves (The unit of C is ppm).

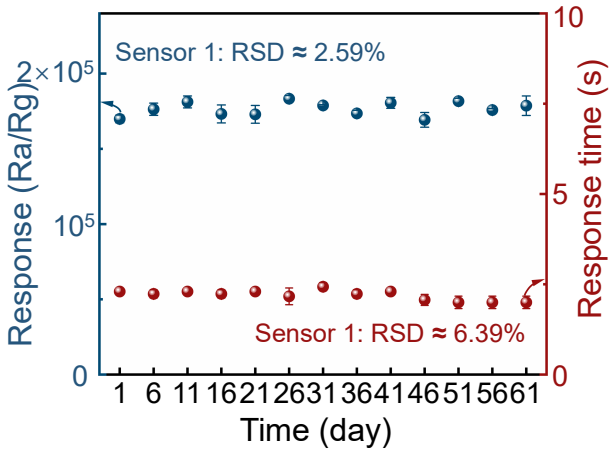

Supplementary Figure 22| The response and response time of the PdO/WO_3-20s sensor to 1000 ppm H_2 at 175 ℃ for 2 months.

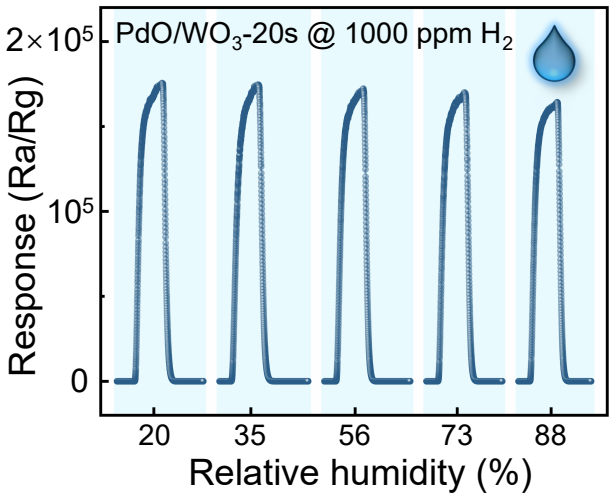

Supplementary Figure 23| The effect of different relative humidities (RH) on the transient response curve of the PdO/WO_3-20s sensor.

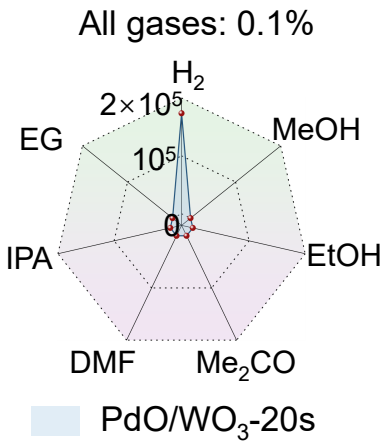

Supplementary Figure 24| Relative responses of PdO/WO_3-20s sensor towards 1000 ppm of various gases at 175 ℃.

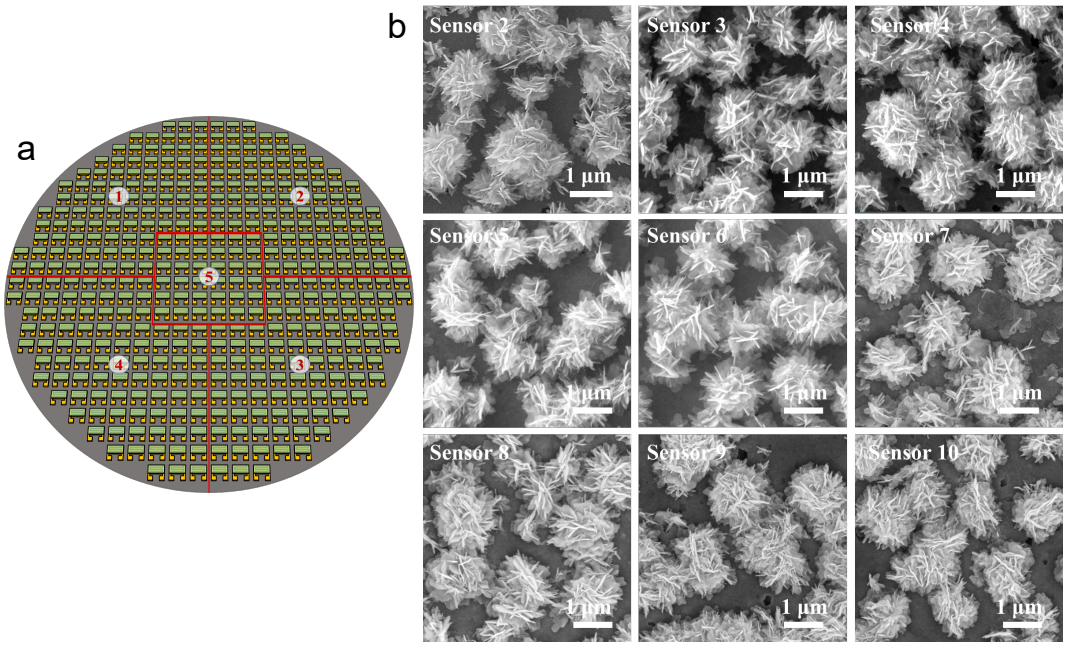

Supplementary Figure 25| a A schematic diagram of the wafer, divided into fiv regions; b Surface morphology of gas sensors (cut from the same wafer) in different regions.

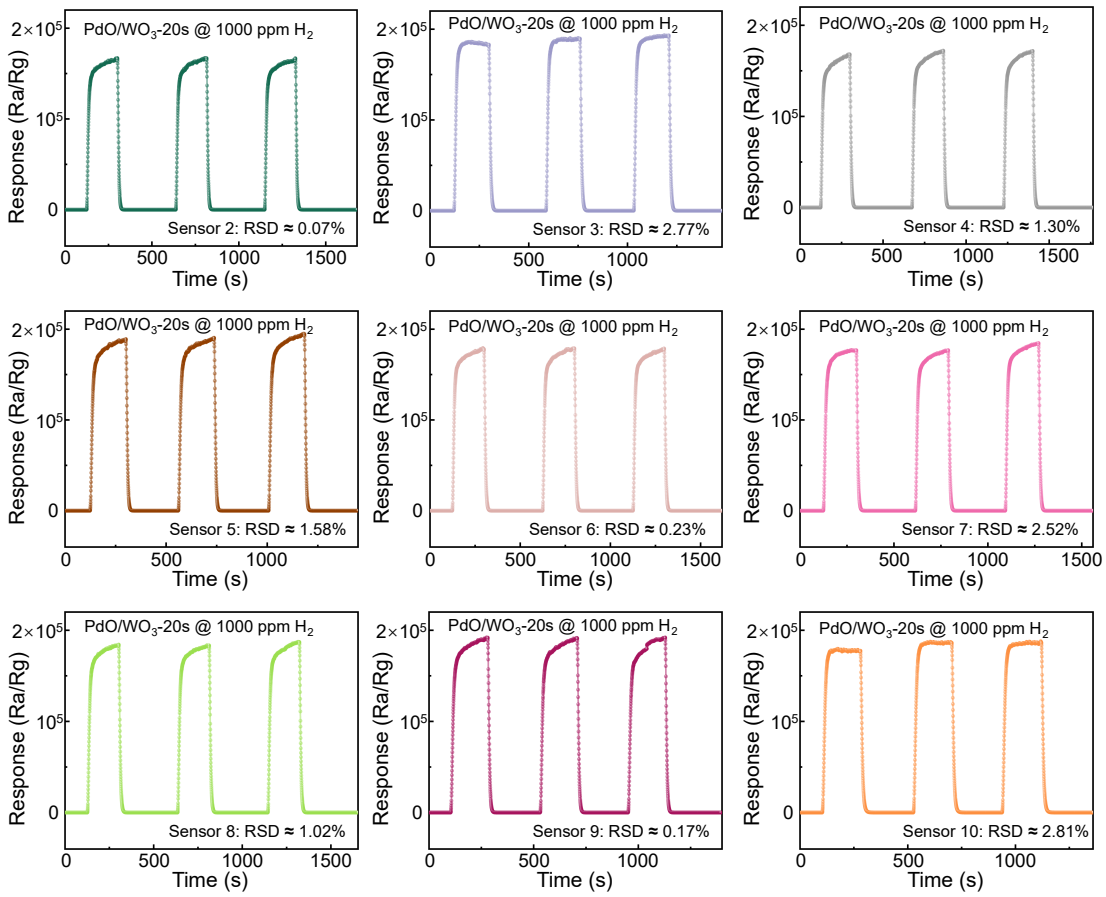

Supplementary Figure 26| Sensor consistency evaluation. The 3-cycle dynamic sensing response of PdO/WO_3-20s sensor from different regions to 1000 ppm H_2.

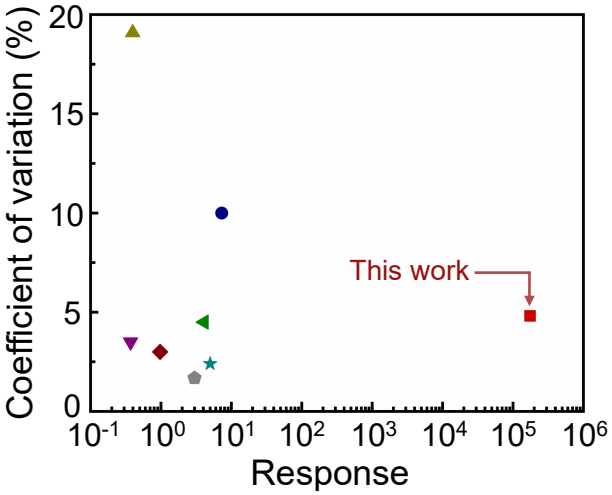

Supplementary Figure 27| Comparison of the responsivity and device-to-device consistency of various wafer-scale devices reported in recent literature.

This figure indicates that our devices retain a high response while exhibiting inter-device consistency comparable to that reported in the literature.

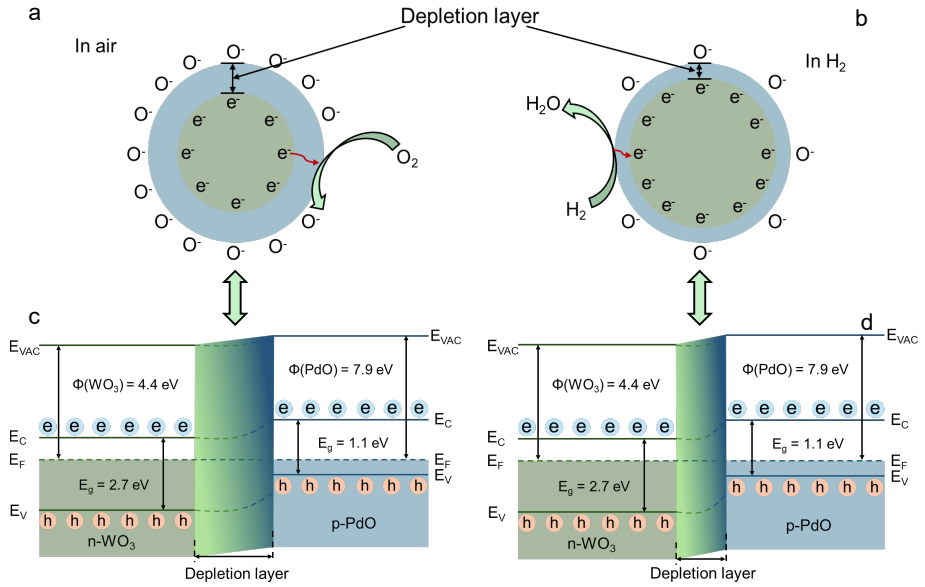

Supplementary Figure 28| The hydrogen sensing mechanism of the PdO/WO_3 sensor. (a, b) Schematic diagrams of the sensing process of PdO-WO_3 exposed to air and H_2 gas, respectively, and the corresponding energy band structures of the PdO-WO_3 nanostructure surface region (c, d).

Hydrogen-sensing mechanism of the PdO/WO_3 sensor

The PdO/WO_3 sensor achieves highly sensitive hydrogen detection through multiple synergistic factors, including the temperature effect, nanoscale effects, the catalytic spillover effect of PdO, and the p–n junction formed between PdO nanoparticles and WO_3 nanostructures. In addition, the innovative microchannel design plays an important role in optimizing gas-detection capability.

It is well known that, when the sensor is exposed to air, oxygen molecules adsorb on the PdO/WO_3 surface. As schematically illustrated in Supplementary Fig. 28(a), across different operating-temperature ranges, oxygen molecules (O_2) capture free electrons from the conduction band of WO_3 and form ionized oxygen species, such as O_2^-, O^-, and O^{2-}[7]. The corresponding reactions can be described by Eqs. (1-4).

$$O_{2(gas)} \rightarrow O_{2(ads.)} \quad (1)$$

$$O_{2(ads.)} + e^- \rightarrow O^-_{2(ads.)} \quad (T < 100\ ℃) \quad (2)$$

$$O^-_{2(ads.)} + e^- \rightarrow 2O^-_{(ads.)} \quad (100\ ℃ < T < 300\ ℃) \quad (3)$$

$$O^-_{(ads.)} + e^- \rightarrow O^{2-}_{(ads.)} \quad (T > 300\ ℃) \quad (4)$$

This process increases the depletion region at the WO_3 surface, thereby raising the baseline resistance. Moreover, temperature strongly influences both the response time and sensitivity of gas sensors: higher temperatures generally accelerate surface reaction rates and

adsorption/desorption kinetics, leading to enhanced responses and shortened response/recovery times[8].

Upon exposure to hydrogen, PdO lowers the activation energy for hydrogen adsorption and catalyses the dissociation of H_2 molecules into H atoms. These H atoms can react with pre-adsorbed oxygen ions (Supplementary Fig. 28(b)), releasing additional free electrons back to the conduction band and thus decreasing the sensor resistance[9]. This process is represented by Eqs. (5, 6).

$$H_2(\text{ad}) \rightleftharpoons 2H(\text{atom}) \quad (5)$$

$$O^-_{(ads.)} + 2H(\text{atom}) \rightleftharpoons 2H_2O + e^- \quad (6)$$

In addition, Pd loading increases the concentration of oxygen vacancies (O_V) on the material surface, as confirmed by the XPS results discussed above. Oxygen defects provide additional reactive sites, enabling more adsorbed oxygen to participate in reactions with hydrogen, inducing larger resistance changes and thereby improving the sensor response[10]. Furthermore, the dissociated H atoms can diffuse to the WO_3 nanosheet surface via the spillover effect, and may further intercalate into the WO_3 lattice to form "HWO_x"[11, 12]. The corresponding reactions can be described by Eqs. (7, 8).

$$H(\text{atom}) \rightleftharpoons H^+ + e^- \quad (7)$$

$$xH^+ + xe^- + WO_3 \rightleftharpoons H_xWO_3 \quad (8)$$

These reactions reduce the oxidation state of W lattice sites and increase the electron concentration in this n-type oxide (thereby lowering the sensor resistance)[13, 14].

The nanoscale characteristics of the PdO/WO_3 hybrid also play a crucial role in enhancing sensing performance. PdO and WO_3 in nanostructured forms possess large surface areas, which increases the number of available active sites and facilitates more gas–surface reactions[15]. In addition, the microchannel design—an innovation of the PdO/WO_3 sensor—substantially strengthens the interaction between gas molecules and the sensing material. These microchannels enable gas to fully access the sensing surface and reduce "dead-zone" areas, thereby increasing the probability of gas adsorption and reaction. By establishing well-defined flow pathways, the microchannel architecture lowers diffusion resistance and ensures rapid and efficient gas transport to and from the reactive interface, which shortens response times and improves detection performance.

Finally, the p–n junction formed between PdO nanoparticles and WO_3 nanostructures constitutes another important component of the sensing mechanism. When a PdO–WO_3 p–n heterostructure forms, the two oxides have different work functions (WO_3: Φ = 4.40 eV; PdO: Φ = 7.90 eV), and free electrons tend to transfer from the side with higher Fermi level to the side with lower Fermi level until a common equilibrium Fermi level is established[4]. During this process, the WO_3 nanosheets near the heterointerface lose additional electrons, resulting in a wider depletion layer (Supplementary Fig. 28(c)) and a higher baseline resistance[16]. When hydrogen adsorbs on the PdO/WO_3 surface, it reacts at oxygen-vacancy-related sites and alters

the electronic structure at the p–n junction, leading to a decrease in sensor resistance (Supplementary Fig. 28(d)). The interaction between PdO and WO_3 further enhances charge-transfer efficiency, amplifies the electrical signal, and increases the hydrogen sensitivity.

In summary, the hydrogen sensitivity of the PdO/WO_3 nanohybrid sensor is jointly determined by the temperature effect, nanoscale features and microchannel design, the catalytic spillover effect of PdO, and the p–n junction formed between PdO and WO_3. The combined action of these factors enables stable operation with high sensitivity and rapid response.

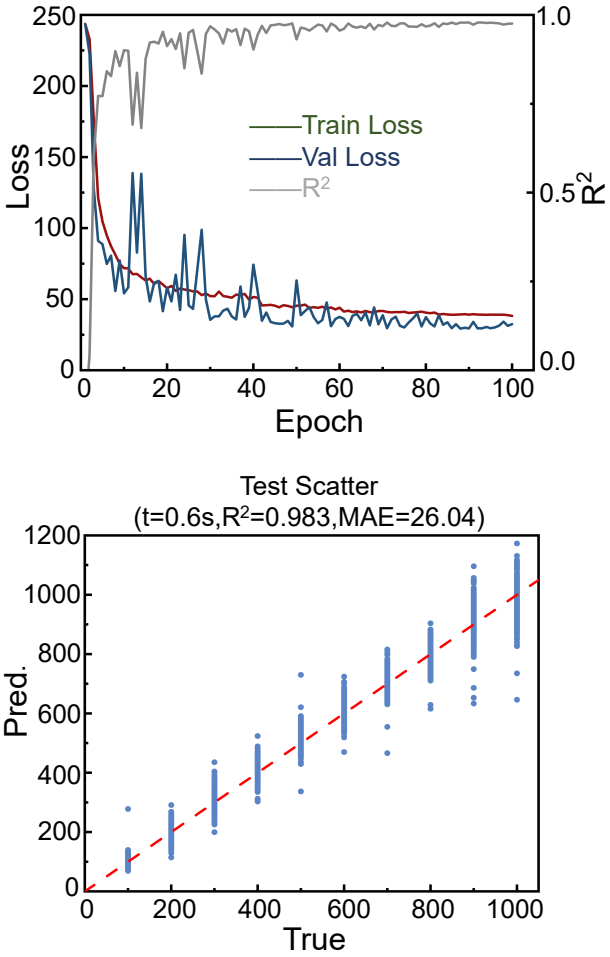

Supplementary Figure 29| Training dynamics and testing performance of the adapted Patch-Transformer.

Training curves: Synchronized convergence of training and validation L1 losses over 100 epochs, alongside the rising validation R^2. The tight alignment of loss curves confirms robust learning without overfitting. Testing scatter plot: Comparison between predicted and actual concentrations on the test set. Data points tightly hug the identity line (y=x), demonstrating high-precision prediction ($R^2 > 0.98$) even with short transient inputs.

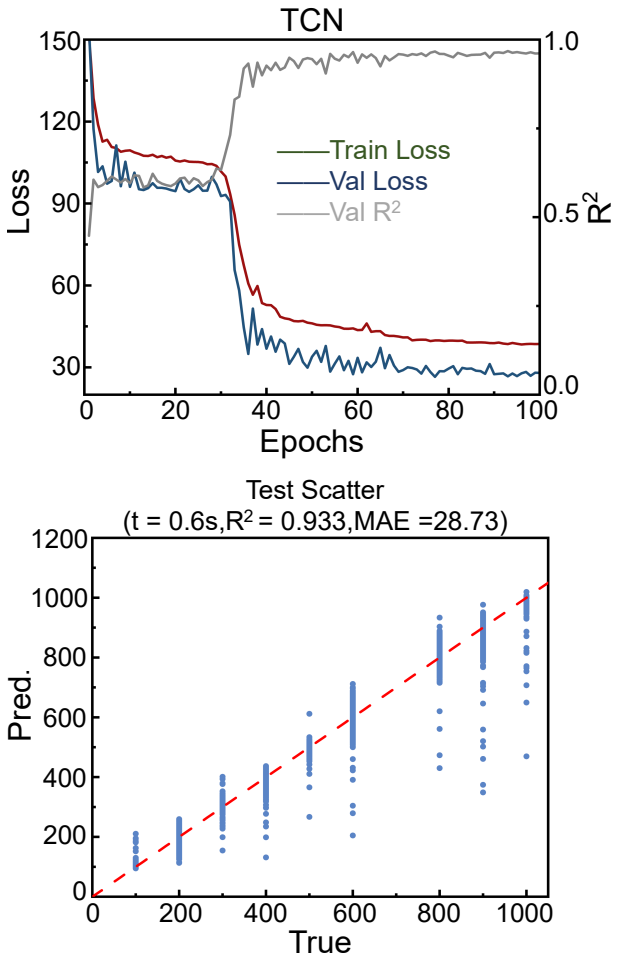

Supplementary Figure 30| Performance evaluation of the TCN architecture.

The learning curves exhibit a comparatively sluggish convergence profile, indicating optimization challenges in capturing short-term signal features. Despite maintaining a respectable validation R^2, the testing scatter plot reveals significant dispersion, with distinct outliers deviating from the identity line. This highlights the instability of the TCN architecture in resolving atypical transient fluctuations compared to the Transformer-based approach.

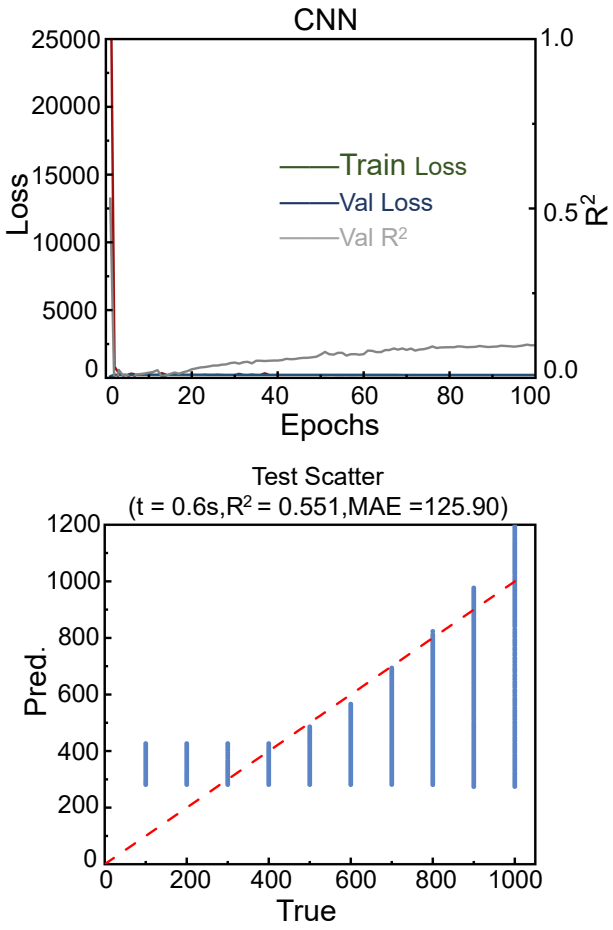

Supplementary Figure 31| Performance evaluation of the CNN architecture.

Both training and validation loss curves plateau at elevated levels with sluggish decay, indicating significant underfitting and an inability to effectively learn the underlying data patterns. The testing scatter plot exhibits substantial dispersion, with a large proportion of samples deviating severely from the identity line. This confirms that a pure convolutional architecture is inadequate for establishing a valid mapping between short-term transient signals and gas concentrations.

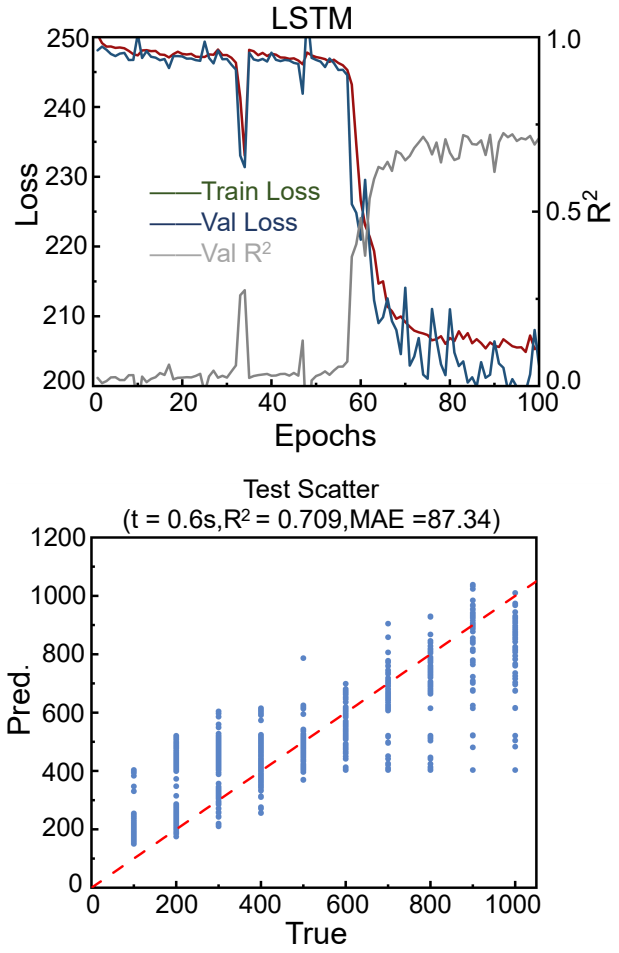

Supplementary Figure 32| Performance evaluation of the LSTM architecture.

The training trajectory exhibits a protracted convergence profile, indicating inefficiencies in gradient optimization for short-term feature extraction. The testing scatter plot reveals considerable dispersion, particularly at higher concentrations, confirming that the recurrent architecture lacks the requisite sensitivity and stability to accurately resolve such ultra-short transient signals.

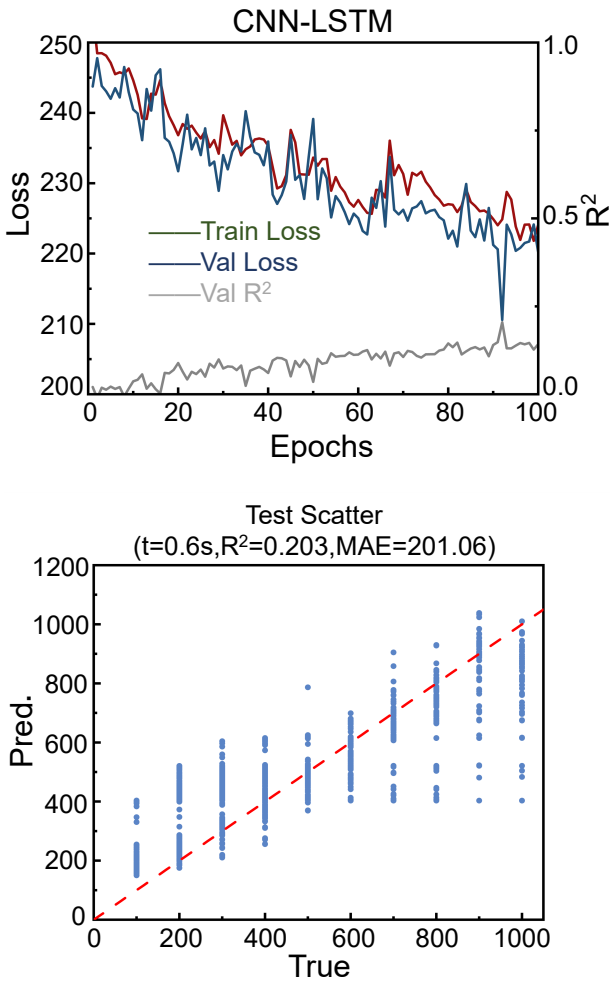

Supplementary Figure 33| Performance evaluation of the CNN-LSTM architecture.

The hybrid architecture exhibits poor convergence performance, with both training and validation losses failing to reach effective minima. The final error is significantly higher than all other baselines, indicating that the inclusion of the LSTM structure induces detrimental interference for short-term signal processing. The testing scatter plot reveals excessive prediction bias and dispersion, confirming the failure of this complex architecture to establish valid feature mapping within the 0.6 s micro-window.

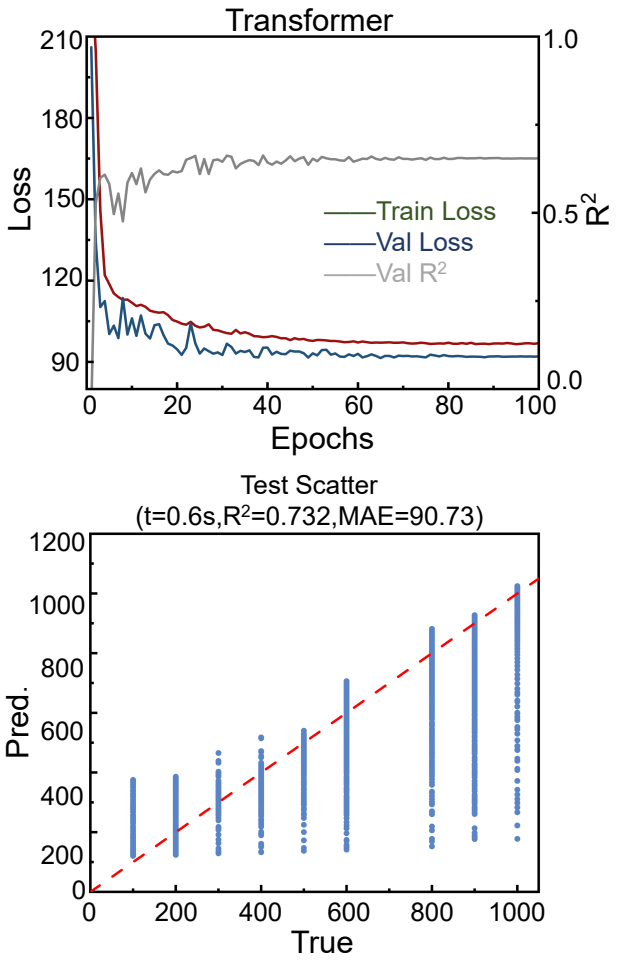

Supplementary Figure 34| Performance evaluation of the standard Transformer architecture.

The model employs a point-wise attention mechanism without patch embedding. The learning curves indicate that both convergence speed and final accuracy fall short of the adapted Patch-Transformer. While the self-attention mechanism establishes global dependencies, the testing scatter plot reveals moderate dispersion. This suggests that without local feature aggregation (patching), the model remains susceptible to signal noise.

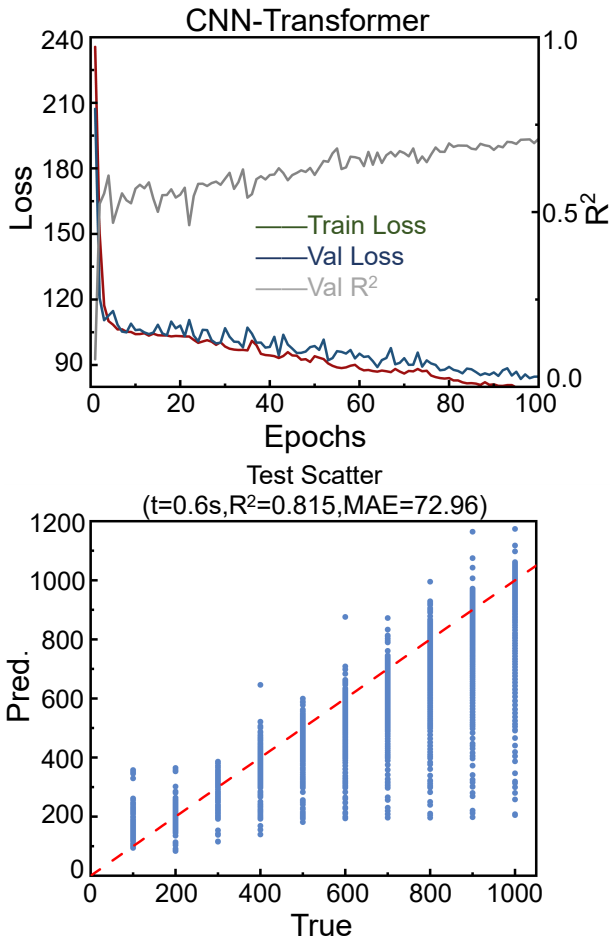

Supplementary Figure 35| Performance evaluation of the CNN-Transformer architecture.

This hybrid model attempts to synergize convolutional feature extraction with self-attention mechanisms. The learning curves show a slightly faster convergence compared to the standard Transformer, validating the contribution of convolutional layers in local feature extraction. However, the testing scatter plot fails to demonstrate a significant accuracy breakthrough, still exhibiting noticeable prediction divergence. This suggests that naive module stacking does not resolve the core challenges of short-term sequence modeling and instead increases optimization complexity.

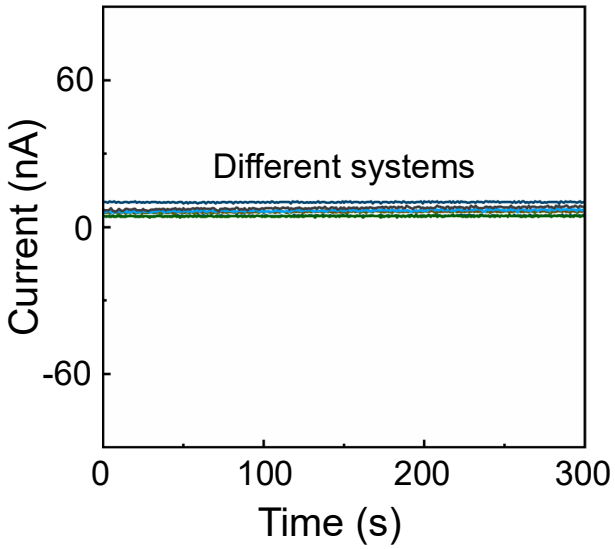

Supplementary Figure 36| The entire system exhibits excellent output consistency.

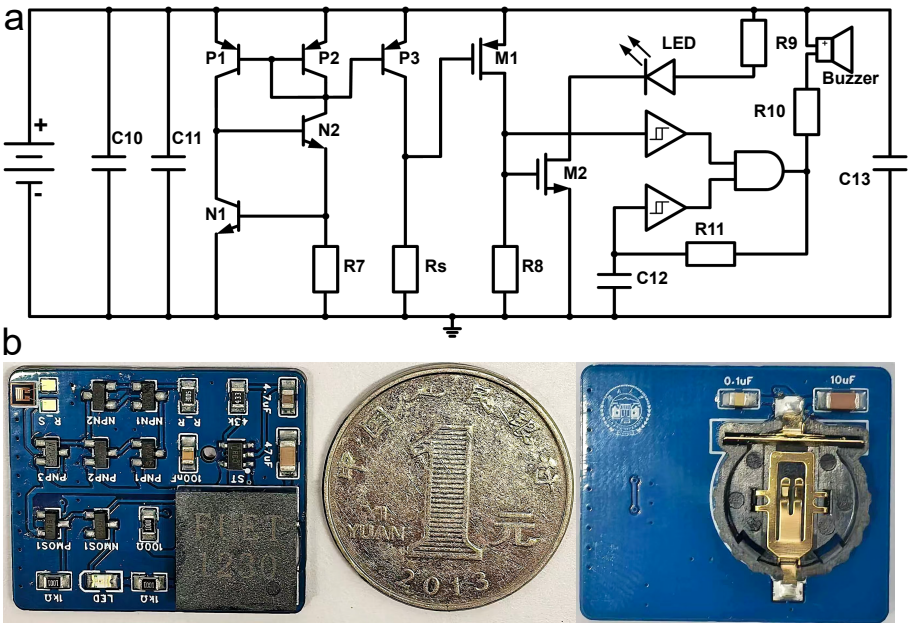

Supplementary Figure 37| Hydrogen leak detection system. a Circuit diagram for hydrogen leakage monitoring. b Actual product image. When the sensor detects a hydrogen leak, the alarm module is activated: the LED turns on and the passive buzzer emits an alarm sound.

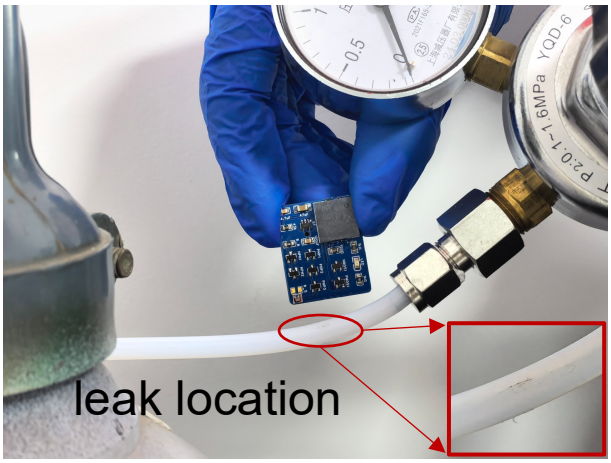

Supplementary Figure 38| Experimental setup used to emulate a realistic hydrogen pipeline leak and demonstrate the alarm device; the leak location is highlighted (red circle), and the inset shows a magnified view of the damaged section of the tubing.

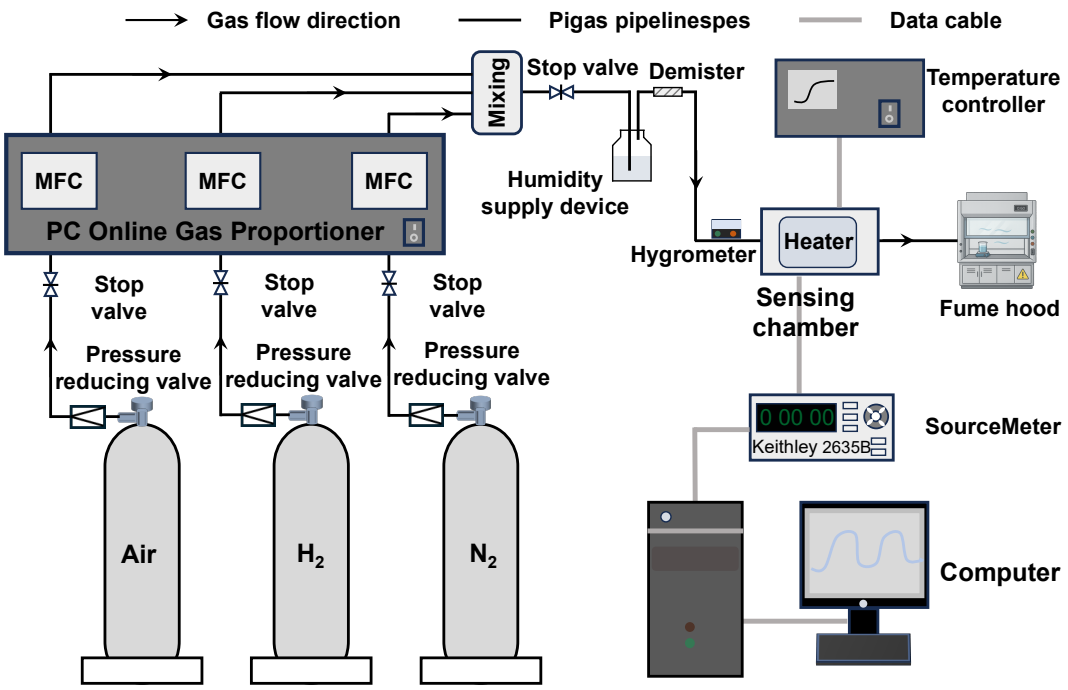

Supplementary Figure 39| Schematic diagram of the dynamic gas distribution system for H_2 sensing tests.

Supplementary Figure 40| Two commercially available humidity sensors were used to measure the actual humidity of the air entering the test chamber.

To ensure traceability of the inlet conditions and the reliability of the measurements, two calibrated commercial hygrometers were positioned at the test-chamber inlet to provide parallel monitoring of the incoming gas and an independent verification of its relative humidity prior to each experiment.

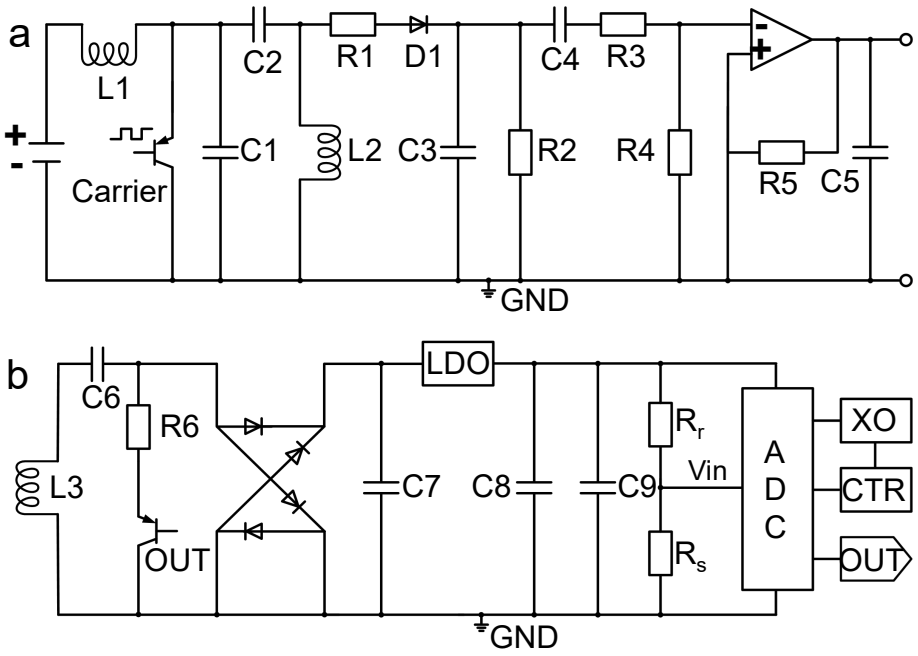

Supplementary Figure 41| The Schematic circuit diagram of circuit board. a Master circuit Schematic, b Slave circuit Schematic.

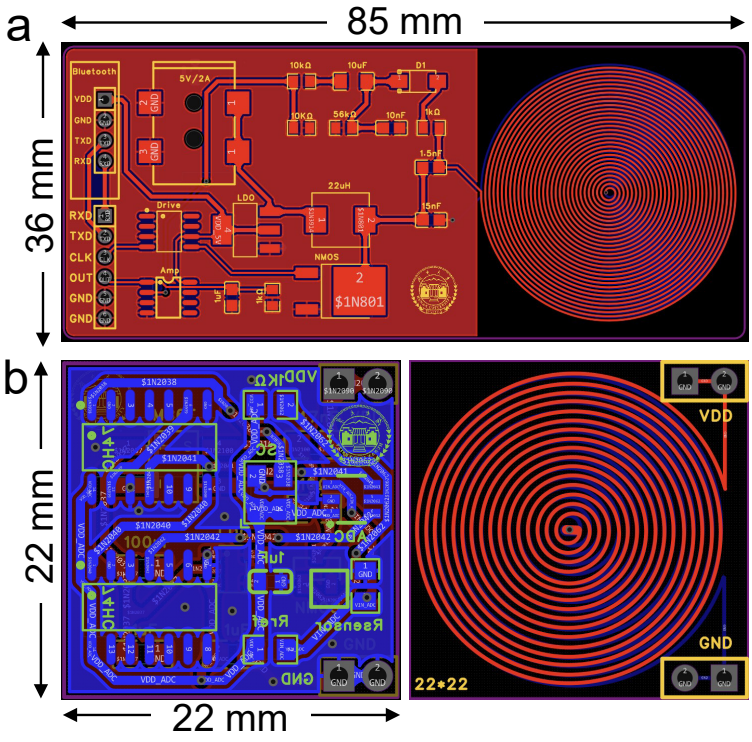

Supplementary Figure 42| The layouts of the printed circuit board (PCB) . a Master circuit PCB, b Slave circuit PCB.

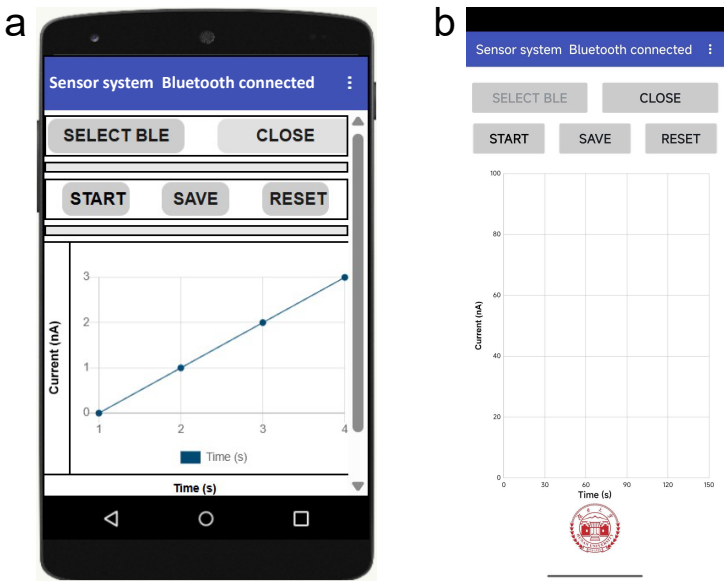

Supplementary Figure 43| User interface of the developed gas-sensing application: (a) component design view in (MIT) App Inventor; (b) screenshot of the mobile app interface.

Supplementary Table 1| Calculation details of the transformation from $WO_3 \cdot H_2O$ to $WO_3 \cdot 2H_2O$.

Lattice parameters of $WO_3 \cdot H_2O$ (the unit cell contains 4 $WO_3 \cdot H_2O$, i.e. 4 W atoms)					
a (Å)	b (Å)	c (Å)	α (°)	β (°)	γ (°)
5.09655	5.33168	10.48044	90.0000	90.0000	90.0000
Lattice parameters of $WO_3 \cdot 2H_2O$ (the unit cell contains 16 $WO_3 \cdot 2H_2O$, i.e. 16 W atoms)					
a (Å)	b (Å)	c (Å)	α (°)	β (°)	γ (°)
10.38471	13.10491	10.47853	90.0000	90.7579	90.0000
Specific energy calculation data					
$4[WO_3 \cdot H_2O]$		-208.46183		-52.1154575	
H_2O		-14.365985		-14.365985	
$16[WO_3 \cdot 2H_2O]$		-1071.125		-66.9453125	
Formation energy (eV)		$\Delta E = E(WO_3 \cdot 2H_2O) - [E(WO_3 \cdot 2H_2O) + E(H_2O)] = -0.46387$			

After $WO_3 \cdot H_2O$ adsorbs water molecules and becomes $WO_3 \cdot 2H_2O$, the number of water molecules between WO_3 layers increases, and the fluctuation of W atoms in the z direction becomes smaller. At the same time, the hydrogen bond interaction between water molecules will change the orientation of water molecules, and the overall structural symmetry will decrease. The negative formation energy indicates $WO_3 \cdot 2H_2O$ is more stable in energy.

Supplementary Table 2| EDS element ratios of W, O, and Pd at different Pd deposition times.

Element	Atom No.	At. %						Normalized wt. %						wt. % Sigma					
		0 s	5 s	10 s	15 s	20 s	25 s	0 s	5 s	10 s	15 s	20 s	25 s	0 s	5 s	10 s	15 s	20 s	25 s
W	74	29.8	27.8	26.4	30.4	29.5	27.0	83.0	80.92	79.12	81.54	80.16	77.41	0.29	0.42	0.47	0.36	0.36	1.29
O	8	70.2	71.6	72.5	68.0	68.1	69.9	17.0	18.13	18.91	15.88	16.10	17.42	0.29	0.32	0.36	0.26	0.25	0.87
Pd	46	0	0.6	1.1	1.7	2.4	3.1	0	0.95	1.97	2.58	3.74	5.16	0	0.32	0.36	0.28	0.28	1.02

Supplementary Table 3| Determine the percentages of elements O_L, O_V, and O_{ad} in the samples at 11-15min-0s and 11-15min-20s by XPS.

11-15min-0s			
Valence	Peak area	Percentage (%)	Proportional value
O_L	14515.36	71.69	71.7
O_V	2577.36	12.73	12.7
O_{ad}	3155.86	15.59	15.6
11-15min-20s			
Valence	Peak area	Percentage (%)	Proportional value
O_L	192666.26	32.3	32
O_V	124247.33	20.8	21
O_{ad}	278810.55	46.8	47

Supplementary Table 4| Percentage of element Pd^0, Pd^{2+} and Pd^{4+} determined from XPS.

Valence	Peak area	Percentage (%)	Proportional value
Pd^0	69254.70	16.8	2
Pd^{2+}	307752.20	74.8	9
Pd^{4+}	34572.8	8.4	1

Supplementary Table 5| Comparison of the performance of different wafer-level gas sensing devices.

Active materials	Synthesis method	Gas	Temp. (℃)	Conc. (ppm)	Response	Response time (s)	RSD	Ref.
PdO/WO_3 nanosheets	**Magnetron sputtering and Chemical etching**	**H_2**	**175**	**1000**	**$1.74*10^5$ Ra/Rg**	**2.3**	**4.45%**	**This work**
Pd NPs/Si nanoforest	Electron beam evaporation	H_2	RT	10000	1685% Rg/Ra*100%	376	1.15%	[17]
Pd-Ni alloy layered film	Electron beam evaporation	H_2	70	10000	~0.6% ΔR/Ra*100%	1	--	[18]
Pt NPs-d-microporous SnO_2	Template method	H_2S	250	20	555.70 Ra/Rg	45.6	--	[19]
Pd-Ni alloy film	Magnetron cosputtering	H_2	75	40000	~2.3% ΔR/Ra*100%	1.5	--	[20]
Rh/SnO_2	Colloidal polymer-directing	C_2H_5OH	300	5	~12.5 Ra/Rg	--	2.4−5.6 %	[21]
Pd NPs	Electron beam evaporation	H_2	RT	1000	$4.86*10^6$ % ΔR/Ra*100%	51.84	--	[22]
μLED-integrated SnO_2 NPs	Hydrothermal	NO_2	--	5	6928 ΔR/Ra	47	--	[23]
In_2O_2-decorated SnO_2 nanosheets	Hydrothermal	Aniline	290	70	7.3 Ra/Rg	--	< 10%	[24]
Pd/SnO_2	Magnetron sputtering and ALD	H_2	150	500	~16 Ra/Rg	--	1.68%	[25]
CNT	Microwave synthesis	H_2	75	300	368% ΔI/Ia*100%	15	--	[26]
Pd/WS_2	Electron beam evaporation	NO_2	RT	1	~11% ΔI/Ia*100%	--	--	[27]
Pt/Y_2O_3	Magnetron sputtering and Electron beam evaporation	H_2S	150	1	97.3% ΔI/Ia*100%	--	~3%	[28]
SnO_2	Magnetron sputtering	H_2	400	400	4 Ra/Rg	--	--	[29]
Pd	Block copolymer self-assembly	H_2	RT	40000	~12.4% Rg/Ra	16	--	[30]

SnO_2	Hydrothermal	C_2H_5OH	300	500	4.1 Ra/Rg	--	~4.5%	[31]
3D graphene	MOCVD	NO_2	RT	5	~15% ΔR/R0*100%	--	--	[32]
CNT	Solution-derived	H_2	RT	20	~140% ΔR/R0*100%	~ 9	--	[33]
Pd-GaN-HN	Magnetron sputtering	H_2	70	1000	7.88% ΔC/C0*100%	1.3	--	[34]
MWCNTs	Spray coating	H_2	420	100000	1.82% ΔR/R0*100%	39	--	[35]
SnO_2	RF sputtering	C_2H_6	RT	50	11.66 Rg/Ra	< 1	--	[36]
Pt-decorated graphene	E-beam evaporator	NH_3	27	50	8% ΔR/Ra*100%	--	19.09%	[37]
In_2O_3	Magnetron sputtering	H_2S	180	50	263% ΔI/Ia*100%	--	--	[38]
NiO	In-situ growth	H_2S	200	5	0.35-0.37 ΔV/Vg	--	< 3.5%	[39]
Ga_2O_3-WO_3	ALD	C_2H_5OH	275	100	14 Ra/Rg	3	--	[40]

Supplementary Table 6| Performance comparison with prior studies under 1000 ppm H_2, with this work indicated.

Materials	Synthesis method	Temperature (℃)	Response	Response Time (s)	Wafer-level	Year	Ref.
PdO/WO_3 nanosheets	**Magnetron sputtering and Chemical etching**	**175**	**1.74×10^5 Ra/Rg**	**2.3**	√	--	**This work**
DPP-DTT	Spin-coating or printing	RT	1.19×10^4 $\Delta R/R_0$	0.84	×	2025	[41]
Pd-In_2O_3 (In_2O_3 microspheres)	Hydrothermal method	80	50.743 Ra/Rg	80	×	2024	[42]
Pd_8SR_{16}–SDBS–rGO （Thiolate-protected Pd nanoclusters (Pd_8SR_{16})）	Solution method	RT	4.48% ± 0.11% ΔR /Ra*100%	0.95	×	2024	[43]
Pd-Si NWs-NAG (FET) (Pd NPs)	Electron beam evaporation	RT	4.86×10^6 % ΔR /Ra*100%	51.84	√	2024	[22]
Pd-WO_3/WS_2 Nanoflowers	Hydrothermal	125	4227.35	1	×	2024	[4]
Pd-WO_3（WS_2 films）	RF-magnetron sputtering	200	586 Ra/Rg	360	×	2023	[44]
Ni-CuO（Pure and nickel doped copper oxide thin films ）	Spray pyrolysis method	300	15.7% ΔI/Ia×100%	459.4	×	2023	[45]
(MoS_2/GR) (MoS_2 spherical nanoparticles with 2D graphene layer)	Facile hydrothermal method	RT	8.1% ΔR/Ra*100%	32	×	2022	[46]
Pd-α-MoO_3 (α-MoO_3 with vertical nanowalls)	Magnetron sputtering and postoxidation	100	3.3×10^5 Ig/Ia	379	×	2022	[47]
Pd(0.5%)-Fe_2O_3/rGO (Pd-loaded α-Fe_2O_3 particles)	Hydrothermal	180	78.4% ΔR/Ra*100%	19s	×	2022	[48]
Orthorhombic Nb2O5−x nanobelts (NBs) with Pt/Ti electrode	Hydrothermal, ion exchange, and annealing treatment	RT	~1.32 Rg/R0	28	×	2022	[49]
Copper thiocyanate (CuSCN)	Solution-processed	RT	1.79 ΔI/Ia*100%	402	×	2022	[50]

PdO-PdAu ternary hollow shells	Template Method	RT	—— ΔR/R0	2.2	×	2022	[51]
WO_3-TiO_2 (WO_3-TiO_2 heterostructural nanofibers (HNFs))	Simple spin coating method	RT	78.21±0.35% ΔR/Ra*100%	20	×	2021	[52]
TiO_2/PVP NFs (TiO_2/PVP nanofibers (NFs))	Electrospinning method	RT	63% ΔI/Ia*100%	89.4	×	2021	[53]
Pd/SnO_2 (SnO_2 films)	ALD	RT	≈ 144.2 Ra/Rg	——	×	2021	[54]
Pt-GaN (FET) (GaN honeycomb nanonetwork)	Layer by molecule beam epitaxy	120	16.7% ΔI/Ia*100%	<= 3	×	2021	[55]
Honeycomb nanonetwork structure (GaN-HN)	Molecular beam epitaxy technique	70	7.88% ΔC/C0*100%	1.3	√	2021	[34]
rGO/SnO_2/PVDF (rGO, SnO_2 and polyvinylidene fluoride (PVDF) tertiary nanocomposite thick film)	Hot press method and E-beam evaporation	RT	71.4% ΔR/Ra*100%	52	×	2020	[56]
Pd-WO_3 Porousfilm	Sol-gel	250	956.52 Ra/Rg	~7	×	2020	[57]
Nanograined Pd or Pd@Pt coated high density electrospun nanofibers, on which	Electrospun, yarn spinning followed by sputter deposition	RT	0.65% ΔR/R0	44	×	2019	[58]
SnO_2（mesoporous SnO_2 (m-SnO_2) powders）	Sol-gel method	400	22.2 Ra/Rg	105	×	2017	[59]
Pd/SnO_2 (Pd nanoparticles composited SnO_2 microspheres)	Solvothermal method	200	129.08 Ra/Rg	——	×	2017	[60]
WO_3/SnO_2 Porous film	Sol-gel	225	29.31 Ra/Rg	8.4	×	2017	[61]
Pd NWs@ZIF-8_4 h (Pd nanowires)	LPNE	RT	0.7% △R/R0*100%	30	×	2017	[62]
Pd NWs@ZIF-8_2 h (Pd nanowires)	LPNE	RT	0.3% △R/R0*100%	13	×	2017	[62]

SnO_2 (nanocrystalline SnO_2 thin film)	Sol–gel method	RT	120% △G/G0*100	214	×	2016	[63]
Pd-WO_3 Nanoplates	Hydrothermal	80	169.3 Ra/Rg	42.8	×	2015	[64]
Pd/WO_3 Nanoplates	Solvothermal	RT	34 Ra/Rg	24	×	2014	[65]
Pd/WO_3 Nanowires	Close-spaced chemical vapor deposition	300	3.1 Ra/Rg	75.6	×	2013	[66]
Pd/WO_3 Nanowires	Hydrothermal	200	140±70%/ppm ΔG/G0×100%	——	×	2013	[67]
Pt/WO_3 Nanoparticles	Flame spray pyrolysis	150	2.58×10^3 Ra/Rg	within a few seconds	×	2011	[68]
WO_3 Nanodots	Electrochemical anodising	150	103 Ra/Rg	~240	×	2010	[69]
Pd/SnO_2 nanowires (Pd–SnO_2 composite nanofibers)	Electrospinning technique and calcination procedure	280	~25 Ra/Rg	~9	×	2010	[70]

Supplementary Table 7| Detailed configuration of experimental protocols. This table outlines the specific settings for the Standard (Full) and Concentration-Holdout evaluation scenarios. For each scenario, the table specifies the concentration levels used for training ("Seen") and those reserved exclusively for testing ("Unseen") to assess the model's robustness against distribution shifts. The "Random Seeds" column lists the specific initialization seeds used to generate the n=4 independent trials for each configuration, ensuring the reproducibility of the statistical results reported in Fig. 4.

Scenario Group	Scenario Name	Seen Concentrations (Training)	Unseen Concentrations (Test Only)	Random Seeds
3-Holdout	H300_600_900	All available concentrations except 300, 600, 900	300, 600, 900 ppm	56,63
3-Holdout	H200_500_800	All available concentrations except 200, 500, 800	200, 500, 800 ppm	56，63
4-Holdout	H200_400_600_800	All available concentrations except 200, 400, 600, 800	200, 400, 600, 800 ppm	56 ， 63
4-Holdout	H300_500_700_900	All available concentrations except 300, 500, 700, 900	300, 500, 700, 900 ppm	56,63
Full (Regular)	No Holdout	All concentrations	None (Test set follows training distribution)	56,57,64,72

Supplementary Table 8| Relative humidity (RH) environments of saturated aqueous salts solutions.

Saturated salt solution	Relative humidity at room temperature	Solubility at 25 °C (~g/100 ml of water*[1])	Theoretical salt dosage（g）	Actual salt mass*[2] (g)	Deionized water volume (mL)
LiCl	11% RH	84.5	253.5	266.2	300ml
$MgCl_2$	33% RH	56.0	168	176.4	
$Mg(NO_3)_2$	53% RH	71.2	213.6	224.3	
NaCl	75% RH	36.0	108	113.4	
K_2SO_4	97% RH	12.0	36	37.8	

*[1] Although solubility is formally reported as grams of solute per 100 g of solvent, the density of deionized water at 25 °C is ≈ 1.0 g mL^{-1}; accordingly, 100 g ≈ 100 mL, and we report the values as g/100 mL.

*[2] The actual salt mass is set 5% higher than the stoichiometric mass for a saturated solution to ensure the system remains at saturation under minor ambient fluctuations.

Supplementary Table 9| Detailed hyperparameters of the adapted Patch-Transformer model and training protocol.

Category	Hyperparameter	Value / Description
Data Processing	Sampling Frequency	15 Hz
	Input Window Size	0.6 s (9 data points)
	Training Window Stride	0.33 s (5 data points)
	Evaluation Window Stride	0.6 s (9 data points, non-overlapping)
	Label Normalization	Scaled to (divided by 1000 ppm)
Patch Embedding	Patch Length	3 points (0.2 s)
	Patch Stride	points (Non-overlapping)
	Number of Patches	3
Model Architecture	Embedding Dimension	128
	Number of Encoder Layers	4
	Number of Attention Heads	4
	Head Dimension	32
	Feed-Forward Expansion Factor	4
	Activation Function	GeLU
	Normalization	LayerNorm (Pre-Norm configuration)
	Dropout Rate	0.2
	Positional Encoding	Learnable (Trainable Parameter)
Training Protocol	Framework	PyTorch (on NVIDIA RTX 4090)
	Parameter Count	~0.79 Million
	Seed	56
	Optimizer	AdamW
	Initial Learning Rate	1×10^{-3}
	Batch Size	64
	Loss Function	Mean Absolute Error (L1 Loss)
	Total Epochs	100
	Learning Rate Scheduler	ReduceLROnPlateau (Factor=0.5, Patience=10)
	Early Stopping / Selection	Best checkpoint based on Validation Loss

Supplementary Table 10| Summarizes a hyper-parameter ablation over patch granularity and model capacity (embedding dimension D, number of layers L) for our patch-based transformer regressor under the 0.6 s input setting. All variants are trained/evaluated under the same split and optimization settings, and we report test R^2 (↑) and MAE (↓).With a fixed backbone (D=128, L=4), point-wise patching (P=1) leads to a clear performance drop compared to moderate patching (P=3), indicating that local aggregation within short windows is important for this regression task. For P=3, scaling the backbone to a smaller model (D=64, L=2) slightly increases MAE, while a larger model (D=256, L=6) substantially increases parameters without meaningful gains. Therefore, we choose P=3, D=128, L=4 as the baseline, balancing accuracy and model complexity.

Variant	Key Settings (P, D, L)	Parameter Count	R^2 (↑)	MAE (↓)
Baseline	(3, 128, 4)	793 K	0.9824	25.99
Patch -1	(1, 128, 4)	794 K	0.8576	58.56
Tiny model	(3, 64, 2)	100 K	0.9808	27.15
Large model	(3, 256, 6)	4.74 M	0.9824	26.14

Supplementary Table 11| List of cultivation conditions for hydrogen-producing bacteria.

Condition	Cultivation temperature (℃)	Sheep blood	Inoculum dilution
Cond.1	20	√	1:100
Cond.2	37	×	1:100
Cond.3	37	√	1:100
Cond.4	37	√	1:500

Supplementary Video.

Demonstration of a hydrogen leak detection system under actual hydrogen leak conditions.

References

1. Oulhakem, O. et al. Effect of water intercalation into tungsten trioxide structure ($WO_3 \cdot xH_2O$)(x= 0, 1, 2): correlation between structure and photocatalytic performances. *J. Catal.* **427**, 115109 (2023).
2. Abedzadeh, M., Ranjbar, M. & Kameli, P. Fabrication of Pd-decorated tungsten oxide nanoflakes for hydrogen sensors via facile anodizing oxidation method. *Int. J. Hydrogen Energy* **50**, 1325-1334 (2024).
3. Wu, J. et al. Ultrafast response and recovery in advanced H_2 sensing: Self-assembled fruit-leaf-like PdO/WO_3 nanostructures. *Sens. Actuators B: Chem.* **430**, 137339 (2025).
4. Wang, X. et al. Design of ultrahigh-response gas sensor based on $Pd\text{-}WO_3/WS_2$ ternary nanocomposites for ultrafast hydrogen detection. *Sens. Actuators B: Chem.* **401**, 134991 (2024).
5. Li, J. et al. Essential role of lattice oxygen in hydrogen sensing reaction. *Nat. Commun.* **15**, 2998 (2024).
6. Ahmad, N. et al. Recent Advances on the Gas-Sensing Properties and Mechanism of Perovskite Oxide Materials-A Review. *ACS omega* **10**, 13780-13796 (2025).
7. Chang, C. et al. Study of a WO_3 thin film based hydrogen gas sensor decorated with platinum nanoparticles. *Sens. Actuators B: Chem.* **317**, 128145 (2020).
8. Degler, D., Weimar, U. & Barsan, N. Current understanding of the fundamental mechanisms of doped and loaded semiconducting metal-oxide-based gas sensing materials. *ACS Sens.* **4**, 2228-2249 (2019).
9. Wang, Z. et al. Sensitization of Pd loading for remarkably enhanced hydrogen sensing performance of 3DOM WO_3. *Sens. Actuators B: Chem.* **262**, 577-587 (2018).
10. Ding, W. et al. Oxygen defects in nanostructured metal-oxide gas sensors: recent advances and challenges. *Chin. J. Chem* . **38**, 1832-1846 (2020).
11. Cai, L. et al. Highly sensitive H_2 sensor based on PdO-decorated WO_3 nanospindle pn heterostructure. *Int. J. Hydrogen Energy* **45**, 31327-31340 (2020).
12. Watanabe, T. et al. A fiber-optic hydrogen gas sensor with low propagation loss. *Sens. Actuators B: Chem.* **145**, 781-787 (2010).
13. Han, S.-I. et al. Effect of structural changes of Pd/WO_3 thin films on response direction and rate in hydrogen detection. *Sens. Actuators B: Chem.* **404**, 135259 (2024).
14. Pehlivan, E., Granqvist, C. G. & Niklasson, G. A. Impedance spectroscopy of electrochromic hydrous tungsten oxide films. *Electron. Mater.* **2**, 312-323 (2021).
15. Zhang, D. et al. Diversiform metal oxide-based hybrid nanostructures for gas sensing with versatile prospects. *Coord. Chem. Rev.* **413**, 213272 (2020).
16. Guo, M. et al. Fast-response MEMS xylene gas sensor based on CuO/WO_3 hierarchical structure. *J. Hazard. Mater.* **429**, 127471 (2022).

17. Xu, X. et al. High-Performance Hydrogen Sensors for ppb-Level Detection at Room Temperature Using Pd Nanoparticle-Coated Si Nanoforest. *ACS Sens.* **10**, 5781-5790 (2025).
18. Huang, T. et al. Ultrafast (0.3 s) integrated hydrogen leakage sensor system empowered by concentration prediction algorithm. *Chem. Eng. J.*, 166395 (2025).
19. Zhu, L. et al. In Situ Synthesis of Ordered Macroporous Metal Oxides Monolayer on MEMS Chips: Toward Gas Sensor Arrays for Artificial Olfactory. *Small* **21**, e03267 (2025).
20. Yang, R. et al. Ultrafast Hydrogen Detection System Using Vertical Thermal Conduction Structure and Neural Network Prediction Algorithm Based on Sensor Response Process. *ACS Sens.* **10**, 2181-2190 (2025).
21. Chen, K. et al. Active Polymer-Templated Porous Metal Oxide Nanospheres with Tailored Single-Atom Modification for Olfactory Intelligence. *J. Am. Chem. Soc.* **147**, 47616-47626 (2025).
22. Hu, Q. et al. Nanotransistor-based gas sensing with record-high sensitivity enabled by electron trapping effect in nanoparticles. *Nat. Commun.* **15**, 5259 (2024).
23. Nam, G. B. et al. Real-time tunable gas sensing platform based on SnO_2 nanoparticles activated by blue micro-light-emitting diodes. *Nano-Micro Lett.* **16**, 261 (2024).
24. Luo, W., Li, J. & Li, M. MEMS Gas Sensors Based on In_2O_3-Decorated SnO_2 Nanosheets for Aniline Detection. *IEEE Sens. J.* **24**, 29669-29677 (2024).
25. Zhang, Z. et al. Wafer-level manufacturing of MEMS H_2 sensing chips based on Pd nanoparticles modified SnO_2 film patterns. *Adv. Sci.* **10**, 2302614 (2023).
26. Al-Diabat, A. M. et al. Improved Hydrogen Gas sensing performance of Carbon Nanotube Synthesized using microwave oven. *IEEE Sens. J.* **23**, 1033-1041 (2022).
27. Sun, Y. & Zhang, Y. Wafer-scale floating-gate field effect transistor sensor built on carbon nanotubes film for Ppb-level NO_2 detection. *Chem. Eng. J.* **473**, 145480 (2023).
28. Zhan, S. et al. Wafer-scale field-effect transistor-type sensor using a carbon nanotube film as a channel for ppb-level hydrogen sulfide detection. *ACS Sens.* **8**, 3060-3067 (2023).
29. Xue, F. et al. A low power four-channel metal oxide semiconductor gas sensor array with T-shaped structure. *J. Microelectromech. Syst.* **31**, 275-282 (2022).
30. Yang, G. G. et al. Multilevel Self-assembly of block copolymers and polymer colloids for a transparent and sensitive gas sensor platform. *ACS nano* **16**, 18767-18776 (2022).
31. Li, M. et al. Wafer-level patterning of SnO nanosheets for MEMS gas sensors. *IEEE Electron Device Lett.* **43**, 1981-1984 (2022).
32. Nasir, T. et al. Wafer-scale growth of 3D graphene on SiO_2 by remote metal catalyst-assisted MOCVD and its application as a NO_2 gas sensor. *Crystal Growth Design* **22**, 4192-4202 (2022).
33. Liu, F. et al. Toward practical gas sensing with rapid recovery semiconducting carbon nanotube film sensors. *Sci. China Inf. Sci.* **65**, 162402 (2022).
34. Yu, H. et al. Capacitive sensor based on GaN honeycomb nanonetwork for ultrafast and low temperature hydrogen gas detection. *Sens. Actuators B: Chem.* **346**, 130488 (2021).
35. Lee, K. et al. Direct integration of carbon nanotubes on a suspended Pt microheater for hydrogen gas sensing. *J. Mater. Sci.: Mater. Electron.* **32**, 19626-19634 (2021).
36. Lee, D. et al. Advanced recovery and high-sensitive properties of memristor-based gas sensor devices operated at room temperature. *ACS Sens.* **6**, 4217-4224 (2021).

37. Kim, Y. et al. Tailored Graphene Micropatterns by Wafer-Scale Direct Transfer for Flexible Chemical Sensor Platform. *Adv. Mater.* **33**, 2004827 (2021).
38. Shin, W. et al. Low frequency noise characteristics of resistor-and Si MOSFET-type gas sensors fabricated on the same Si wafer with In_2O_3 sensing layer. *Sens. Actuators B: Chem.* **318**, 128087 (2020).
39. Liu, L. et al. "Top-down" and "bottom-up" strategies for wafer-scaled miniaturized gas sensors design and fabrication. *Microsyst. Nanoeng.* **6**, 31 (2020).
40. Wei, Z. et al. Ultra-thin sub-10 nm Ga_2O_3-WO_3 heterostructures developed by atomic layer deposition for sensitive and selective C_2H_5OH detection on ppm level. *Sens. Actuators B: Chem.* **287**, 147-156 (2019).
41. Mandal, S. et al. A robust organic hydrogen sensor for distributed monitoring applications. *Nat. Electron.*, 1-10 (2025).
42. Tang, M. et al. Enhanced H_2 gas sensing performances by Pd-loaded In_2O_3 microspheres. *Appl. Phys. A* **130**, 741 (2024).
43. Chen, Z. et al. Balancing Pd–H Interactions: Thiolate-Protected Palladium Nanoclusters for Robust and Rapid Hydrogen Gas Sensing. *Adv. Mater.* **36**, 2404291 (2024).
44. Mobtakeri, S. et al. Effect of growth pressure on sulfur content of RF-magnetron sputtered WS_2 films and thermal oxidation properties of them toward using Pd decorated WO_3 based H_2 gas sensor. *Sens. Actuators B: Chem.* **381**, 133485 (2023).
45. Güldüren, M. E. et al. Investigating the influence of Ni doping on the CuO thin films deposited via ultrasonic spray pyrolysis: structural, optical and H_2 gas sensing analyses. *Int. J. Hydrogen Energy* **48**, 828-839 (2023).
46. Munusami, V. et al. High sensitivity LPG and H_2 gas sensing behavior of MoS_2/graphene hybrid sensors prepared by facile hydrothermal method. *Ceram. Int.* **48**, 29322-29331 (2022).
47. Mobtakeri, S., Habashyani, S. & Gür, E. Highly responsive Pd-decorated MoO_3 nanowall H_2 gas sensors obtained from in-situ-controlled thermal oxidation of sputtered MoS_2 films. *ACS Appl. Mater. Interfaces* **14**, 25741-25752 (2022).
48. Liu, B. et al. Fabrication of Pd-loaded α-Fe_2O_3 decorated rGO hybrids for highly sensitive H_2 sensing. *Appl. Surf. Sci.* **579**, 152220 (2022).
49. Yang, P. et al. Fast, Sensitive, and highly selective room-temperature hydrogen sensing of defect-rich orthorhombic Nb_2O_{5-x} nanobelts with an abnormal p-type sensor response. *ACS Appl. Mater. Interfaces* **14**, 25937-25948 (2022).
50. Kabitakis, V. et al. A Low-Power CuSCN Hydrogen Sensor Operating Reversibly at Room Temperature. *Adv. Funct. Mater.* **32**, 2102635 (2022).
51. Li, Q. et al. Controllable fabrication of PdO-PdAu Ternary hollow shells: synergistic acceleration of H_2-sensing speed via morphology regulation and electronic structure modulation. *Small* **18**, 2106874 (2022).
52. Kumaresan, M. et al. TiO_2 nanofibers decorated with monodispersed WO_3 heterostruture sensors for high gas sensing performance towards H_2 gas. *Inorg. Chem. Commun.* **129**, 108663 (2021).
53. Al-Hazeem, N. Z. et al. Hydrogen gas sensor based on nanofibers TiO_2-PVP thin film at room temperature prepared by electrospinning. *Microsyst. Technol.* **27**, 293-299 (2021).
54. Song, Z. et al. Wireless self-powered high-performance integrated nanostructured-gas-

sensor network for future smart homes. *ACS nano* **15**, 7659-7667 (2021).
55. Zhong, A. et al. Ultrafast H_2 gas nanosensor for ppb-level H_2 gas detection based on GaN honeycomb nanonetwork. *Sens. Actuators B: Chem.* **329**, 129079 (2021).
56. Punetha, D., Kar, M. & Pandey, S. K. A new type low-cost, flexible and wearable tertiary nanocomposite sensor for room temperature hydrogen gas sensing. *Sci. Rep.* **10**, 2151 (2020).
57. Han, Z. et al. Multilayer porous Pd-WO_3 composite thin films prepared by sol-gel process for hydrogen sensing. *Int. J. Hydrogen Energy* **45**, 7223-7233 (2020).
58. Kim, D.-H. et al. High-resolution, fast, and shape-conformable hydrogen sensor platform: polymer nanofiber yarn coupled with nanograined Pd@Pt. *ACS nano* **13**, 6071-6082 (2019).
59. Xue, N. et al. Highly sensitive and selective hydrogen gas sensor using the mesoporous SnO_2 modified layers. *Sensors* **17**, 2351 (2017).
60. Li, Y. et al. Pd nanoparticles composited SnO_2 microspheres as sensing materials for gas sensors with enhanced hydrogen response performances. *J. Alloys Compd.* **710**, 216-224 (2017).
61. Zhang, Z. et al. H_2 response characteristics for sol–gel-derived WO_3-SnO_2 dual-layer thin films. *Ceram. Int.* **43**, 6693-6699 (2017).
62. Koo, W.-T. et al. Accelerating palladium nanowire H_2 sensors using engineered nanofiltration. *ACS nano* **11**, 9276-9285 (2017).
63. Kadhim, I. H., Hassan, H. A. & Abdullah, Q. Hydrogen gas sensor based on nanocrystalline SnO_2 thin film grown on bare Si substrates. *Nano-Micro Lett.* **8**, 20-28 (2016).
64. Wang, Y. et al. High performance and negative temperature coefficient of low temperature hydrogen gas sensors using palladium decorated tungsten oxide. *J. Mater. Chem. A* **3**, 1317-1324 (2015).
65. Liu, B. et al. Improved room-temperature hydrogen sensing performance of directly formed Pd/WO_3 nanocomposite. *Sens. Actuators B: Chem.* **193**, 28-34 (2014).
66. Chávez, F. et al. Sensing performance of palladium-functionalized WO_3 nanowires by a drop-casting method. *Appl. Surf. Sci.* **275**, 28-35 (2013).
67. Kukkola, J. et al. Room temperature hydrogen sensors based on metal decorated WO_3 nanowires. *Sens. Actuators B: Chem.* **186**, 90-95 (2013).
68. Samerjai, T. et al. Selectivity towards H_2 gas by flame-made Pt-loaded WO_3 sensing films. *Sens. Actuators B: Chem.* **157**, 290-297 (2011).
69. Calavia, R. et al. Fabrication of WO_3 nanodot-based microsensors highly sensitive to hydrogen. *Sens. Actuators B: Chem.* **149**, 352-361 (2010).
70. Zhang, H. et al. Enhancement of hydrogen monitoring properties based on Pd–SnO_2 composite nanofibers. *Sens. Actuators B: Chem.* **147**, 111-115 (2010).